# Short-term orbital effects of radiation pressure on the Lunar Reconnaissance Orbiter

Dominik Stiller

August 2023

Supervised by Dr. Dominic Dirkx

Research paper for the

Honours Programme Bachelor

at the

Faculty of Aerospace Engineering

Delft University of Technology

TU Delft

# Short-term orbital effects of radiation pressure on the Lunar Reconnaissance Orbiter

**Dominik Stiller**

*B.Sc. student, Faculty of Aerospace Engineering, Delft University of Technology, The Netherlands*

**Abstract**

Precision orbit determination for geodetic applications requires force models even for small perturbations. Radiation from the Sun and Moon is a significant source of perturbation in lunar orbits and inadequate modeling of radiation pressure (RP) can lead to large position errors. This paper describes the short-term effect of RP on the Lunar Reconnaissance Orbiter (LRO), which has a position knowledge requirement of 50 m to 100 m in total and below 1 m radially. We compared models of varying complexity to determine the benefits and computational cost of high-accuracy RP modeling. We found that (1) the accelerations differ greatly depending on the Sun position, (2) only a paneled spacecraft model can account properly for changing orientation and geometry of LRO, and (3) a constant-albedo model is sufficient for lunar radiation, which is dominated by the thermal component. A spherical harmonics model for lunar albedo increases computational cost with little gain in the attained accuracy. If RP is neglected, the along-track position errors can be as large as 1100 m and the radial error varies periodically with an amplitude of up to 24 m, highlighting the importance of adequate force modeling to meet LRO's orbit determination requirements.

**Keywords**

Radiation pressure, Lunar Reconnaissance Orbiter, precision orbit determination, force modeling

**Abbreviations**: BRDF: bidirectional reflectance distribution function; DLAM-1: Delft Lunar Albedo Model 1; LRO: Lunar Reconnaissance Orbiter; RMSE: root mean square error; RP: radiation pressure; rRMSE: relative root mean square error; Tudat: TU Delft Astrodynamics Toolbox.

## 1 Introduction

Precision orbit determination is a cornerstone of satellite navigation and spaceborne geodesy. Only if the state, and particularly the position, of the spacecraft are known accurately can the high precision of modern instruments for gravity field recovery or satellite altimetry be exploited fully. Next to tracking data, force models accounting for gravity, solid tides, drag, and other accelerations have the largest role in improving orbit determination. Another important non-conservative force is radiation pressure (RP), which arises from the exchange of momentum between electromagnetic radiation and the spacecraft. Because RP accelerations can have magnitudes similar to third-body and irregular gravity field perturbations [1], neglecting or mismodeling them can deteriorate position knowledge below acceptable levels.

The Lunar Reconnaissance Orbiter (LRO) was launched in June 2009 to identify safe landing sites, locate resources, and characterize the radiation environment for future human missions to the Moon [2]. To fulfill these objectives, LRO is equipped with instruments to create high-resolution maps of the lunar topography and gravity field. Accuracies of $50\,\mathrm{m}$ to $100\,\mathrm{m}$ in the total position and sub-meter accuracy in the radial component are required to take advantage of the instrument resolutions [3, 4], which necessitates force modeling even of small perturbations. Solar RP is the "largest non-gravitational perturbation affecting the LRO orbit and inadequate modeling [...] is the primary cause of large prediction errors for LRO, particularly during high-beta angle periods" [5]. The Moon itself is also a significant radiation source since there is no atmosphere and especially the lunar highlands are reflective [6]. The orbit determination error is also highly dependent on the modeling of how RP translates to accelerations: particularly during full-Sun periods, a model accounting for LRO's geometry and the definitive orientation of the solar array and high gain antenna outperforms a simple spherical model [7].

This paper describes the short-term effects of RP on LRO's orbit and the sensitivities of these effects to models of varying complexity. Other authors have already described their orbit determination approaches for LRO [5, 7–13], but none compared RP modeling choices and their implications. Vielberg and Kusche investigated the effect of different RP models for Earth [14], where a plethora of observations are available and the radiation environment differs greatly from the Moon. Therefore, their results do not apply to orbits around the Moon. Our paper alleviates this lack of guidance for lunar orbits by elucidating the choice of force models for orbit determination both in terms of attainable accuracy and computational performance. The results relate to short-term effects over 2.5 days, which is a typical arc used in orbit determination. Long-term effects, which may cancel or compound over the span of months, are not considered here.

The TU Delft Astrodynamics Toolbox (Tudat) was used for all orbital simulations and the models presented here were integrated into the software, which is freely available at `https://docs.tudat.space/`.

Email: dstiller@uw.edu

## 2 Radiation pressure modeling

RP modeling requires the cooperation of models for the radiation sources and the spacecraft. This section presents a collection of compatible models, starting with a physical description of RP and reflectance, which form the building blocks for models of increasing complexity.

### 2.1 Mechanics of radiation pressure

RP results from the momentum transfer between electromagnetic radiation and a surface. A spacecraft may receive such radiation from the Sun but also from other celestial bodies: planets and moons emit albedo radiation through the reflection of sunlight and thermal radiation depending on the surface temperature. The RP exerts a force on the spacecraft that is governed by surface properties such as area, reflectivity, and absorptivity. The resulting acceleration is the result of a complex interplay of the bodies emitting radiation (the "sources") and the spacecraft affected by the radiation (the "target").

Radiation can be characterized by the radiant flux density, which commonly has units of $\mathrm{W/m^2}$. The radiosity $J$ is the *emitted and reflected* radiant flux density of an opaque surface. The irradiance $E$ is the *incident* radiant flux density on a surface. The RP exerted on an irradiated surface is proportional to $1/c$, where $c = 299\,792\,458\,\mathrm{m/s}$ is the speed of light. Given the magnitude of $c$, RP is usually small (around $4.5 \times 10^{-6}\,\mathrm{N/m^2}$ for solar radiation at Earth, where $E = 1361\,\mathrm{W/m^2}$ [15]).

A light ray emitted by a source can be thought of as an irradiance with a direction. Such directional irradiances provide a convenient way to decouple source and target models: the irradiance and the direction of ray incidence are sufficient to determine the target acceleration, independently of the actual source. Therefore, one or more directional irradiances are the output of a source model and are used as input to the target model. We represent a directional irradiance as vector $\mathbf{E} = E\hat{\mathbf{r}}_{t/s}$, where $\hat{\mathbf{r}}_{t/s}$ is the unit vector in the source-to-target direction.

Electromagnetic radiation is often composed not just of a single wavelength but rather a range of wavelengths. The distribution can be described by the spectral irradiance in units of $\mathrm{W/(m^2\,Hz)}$. Since surface properties are often wavelength-dependent, the target model would also have to be aware of the distribution. However, the surface properties as a function of wavelength are often not known, which is also the case for LRO. Therefore, we assume the irradiance from source models to be integrated over the whole spectrum and the surface properties of the target model to be valid for all wavelengths.

### 2.2 Reflectance distribution

Describing the reflectance of a surface is key to RP modeling. Both the way a source reflects sunlight due to albedo and the direction a target is accelerated in depend on the angular distribution of reflectance.

*General reflectance distribution* In general, reflectance comprises a diffuse (scattered in many directions) and a specular (mirror-like) component. The remaining energy is absorbed by the surface. The reflectance varies with surface normal $\mathbf{N}$, incoming radiation direction $\mathbf{L}$, and observer direction $\mathbf{V}$. This geometry is shown in Figure 1. A bidirectional reflectance distribution function (BRDF) describes the fraction of irradiance reflected toward the observer per steradian, i.e. [16]

$$f_r(\theta_i, \phi_i, \theta_r, \phi_r) = \frac{\mathrm{d}L_r(\theta_r, \phi_r)}{\mathrm{d}E_i(\theta_i, \phi_i)}, \tag{1}$$

where $\mathrm{d}L_r$ is the reflected radiance (the directional counterpart to radiosity, typically in $\mathrm{W/(m^2\,sr)}$) and $\mathrm{d}E_i$ is the received irradiance.

The planetary surface BRDF directly leads to the albedo irradiance received by a target if the solar irradiance at the planet's surface and the solid angle subtended by the target are known.

The target surface BRDF gives the direction in which the target is accelerated through integration over all directions $\mathbf{V}$ in which radiation is reflected. The unitless reaction vector, which includes both the direction and magnitude based on absorbed, specularly reflected, and diffusely reflected fractions, is therefore [16]

$$\mathbf{R} = -\left[\mathbf{L} + \int_0^{2\pi} \int_0^{\pi/2} f_r \cos\theta_r \mathbf{V}\,\mathrm{d}\theta_r\,\mathrm{d}\phi_r\right]. \tag{2}$$

This vector encapsulates the mechanics of momentum transfer. The reaction is minimal for pure absorption ($f_r = 0$) and maximal (double the minimum) for pure specular reflection in the incidence direction.

*Specular–diffuse reflectance distribution* A simplified BRDF is usually more practical for RP modeling: the reflectance is assumed to be a mix of an ideal Lambertian diffuse component and a purely mirror-like specular component. Such a BRDF is given by [16]

$$f_r = C_d \frac{1}{\pi} + C_s \frac{\delta(\mathbf{V} - \mathbf{M})}{\cos\theta_i}, \tag{3}$$

where $\delta$ is the delta function and $C_d$ and $C_s$ are the diffuse and specular reflectivity coefficients. Together with the absorption coefficient $C_a$, energy is conserved if $C_a + C_d + C_s = 1$. The vector $\mathbf{M} = 2\cos\theta_i \mathbf{N} - \mathbf{L}$ is $\mathbf{L}$'s mirror-like reflection, which contributes only if $\mathbf{V} = \mathbf{M}$.

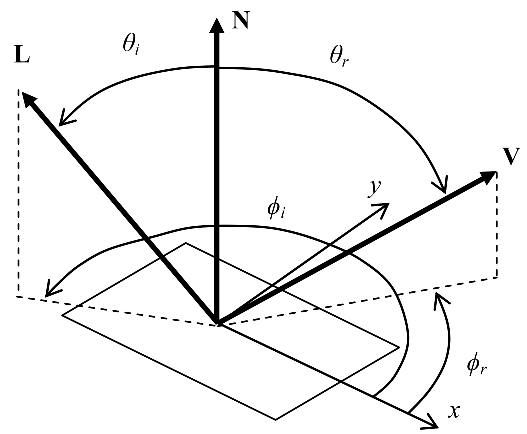


**Figure 1.** Geometry of a BRDF for a surface with normal $\mathbf{N}$, incoming direction $\mathbf{L}$, and observer direction $\mathbf{V}$. The viewing angle $\theta_r$ is between $\mathbf{N}$ and $\mathbf{V}$. The phase angle (not labeled) is between $\mathbf{L}$ and $\mathbf{V}$. Adapted from [16].

For this simplified BRDF, the integral in Equation (2) evaluates to [17]

$$\mathbf{R} = -\left[(C_a + C_d)\mathbf{L} + \frac{2}{3}C_d\mathbf{N} + 2\cos\theta_i C_s \mathbf{N}\right]. \quad (4)$$

Further, when the target is in thermodynamic equilibrium, all absorbed radiation is reradiated instantaneously by Kirchhoff's law. If this reradiation is Lambertian, the reaction vector becomes [17]

$$\mathbf{R} = -\left[(C_a + C_d)\left(\mathbf{L} + \frac{2}{3}\mathbf{N}\right) + 2\cos\theta_i C_s \mathbf{N}\right]. \quad (5)$$

The specular contribution is strictly along the surface normal direction since its tangential components cancel. The Lambertian diffuse contribution (both reflected and reradiated) has a component along the incoming direction but also, weighted by a factor $2/3$ (see [18] for a derivation of this factor), a component along the surface normal. The reaction vector is thus always in the plane spanned by $\mathbf{L}$ and $\mathbf{N}$.

### 2.3 Radiation sources

Radiation sources emit or reflect radiation. As explained in Section 2.1, the incident radiation at a target due to a source can be thought of as light rays, which are described by their directional irradiance at the target. How the directional irradiance is calculated depends on the type of source.

*Isotropic point sources* The simplest source model is a point source that isotropically radiates in all directions. This model is appropriate for far-away sources such as the Sun at $1\,\mathrm{au}$ distance. Due to the distance, all rays are effectively parallel and can be merged into a single ray parallel to the source-to-target vector $\mathbf{r}_{t/s}$. For an isotropic source, the total luminosity $L$ (units of W) is uniformly distributed over a sphere, leading to an inverse square law. Therefore, the irradiance at the target is

$$E = \frac{L}{4\pi\left\|\mathbf{r}_{t/s}\right\|^2}. \quad (6)$$

Alternatively, a reference irradiance $E_{\text{ref}}$ observed at a distance $\mathbf{r}_{\text{ref}}$ can be scaled:

$$E = E_{\text{ref}}\frac{r_{\text{ref}}}{\left\|\mathbf{r}_{t/s}\right\|^2}. \quad (7)$$

The solar luminosity is $3.828 \times 10^{26}\,\mathrm{W}$ [19], which corresponds to an irradiance of $1361\,\mathrm{W/m^2}$ at $1\,\mathrm{au}$. Note that these values are averages, which vary with the 11-year solar cycle by about $0.1\,\%$ and more on shorter timescales due to sunspot darkening and facular brightening [20]. Observational time series exist to account for these variations [21].

*Paneled sources: Discretization* Radiation due to planets and moons requires more involved source models. Planetary emissions comprise reflected solar radiation and thermal infrared radiation [22]. The fraction of reflected sunlight is called albedo[1] $a$; the corresponding type is therefore also called albedo radiation. Thermal radiation is due to absorbed solar energy that is re-emitted in a delayed fashion. Observational time series of albedo and thermal fluxes exist for Earth [21], but physical modeling is required for the Moon.

Since planetary radiation is not isotropic and the spacecraft is typically much closer to the body than to the Sun, the source extent has to be considered. In contrast to the previously described point source, Earth and Moon are, therefore, modeled as extended sources. These are discretized into sub-sources, from which rays emanate that are generally not parallel or of equal power. The sub-sources can be thought of as panels with an area, orientation, position, and radiosity model. The panel extent is represented by the area but any other panel properties are solely evaluated at its center. A panel only radiates from the positive normal side, not from the backside.

Different algorithms exist to divide the planet ellipsoid into panels. Some authors use a longitude–latitude grid (e.g., [24, 25], particularly with observed fluxes) or generate static, uniformly spaced panels over the whole sphere (e.g., [16]). However, both approaches are inefficient for low-altitude spacecraft, which require a large number of panels, most of which are never visible. Therefore, the de facto standard is dynamic[2] paneling as introduced by Knocke *et al.* [22].

In Knocke's method, only the visible area of the planet is paneled. This area is a spherical cap, centered at the subsatellite point and divided into concentric rings that are, again, divided into equal-width segments. A central panel is located at the subsatellite point. All panels contribute to the irradiance received by the target. However, the effective area of each panel is projected by its viewing angle $\theta_r$ (see Figure 1) and the irradiance is attenuated by an inverse square law. In Knocke's method, the rings are spaced such that each panel has the same projected, attenuated area. The projected, attenuated area of a panel is defined as [22]

$$\frac{\mathrm{d}A\cos\theta_r}{\left\|\mathbf{r}_{t/s}\right\|^2}, \quad (8)$$

where $\mathrm{d}A$ is the geometric panel area and $\mathbf{r}_{t/s}$ is the source-to-target vector (in this case, the panel-to-target vector). More rings and more panels per ring improve the fidelity of the calculated irradiance, barring the resolution limit of the radiosity model (e.g., the albedo distribution). While arbitrary numbers of panels per ring are possible, Knocke suggests multiples of 6 (i.e., six panels in the first ring, twelve panels in the second ring, ...). The algorithm is elaborated in [26].

Two examples at different spacecraft altitudes and with different ring numbers are shown in Figure 2. At higher altitudes, a larger area is visible (approaching a hemisphere) and panels are somewhat more uniform in area. At lower altitudes, the panels are more tightly spaced toward the subsatellite point. In both cases, panel areas increase toward

[1] Two types of albedo exist: spherical/Bond albedo is the fraction of sunlight reflected in all directions, while geometrical albedo is the fraction of sunlight reflected with respect to an ideal diffuse surface for normal incidence and viewing directions [23]. For our purpose, spherical albedo is appropriate and synonymous with albedo in this paper.

[2] Dynamic refers to the fact that panels move with the spacecraft, as opposed to static paneling, for which panels are invariant with spacecraft position or time.

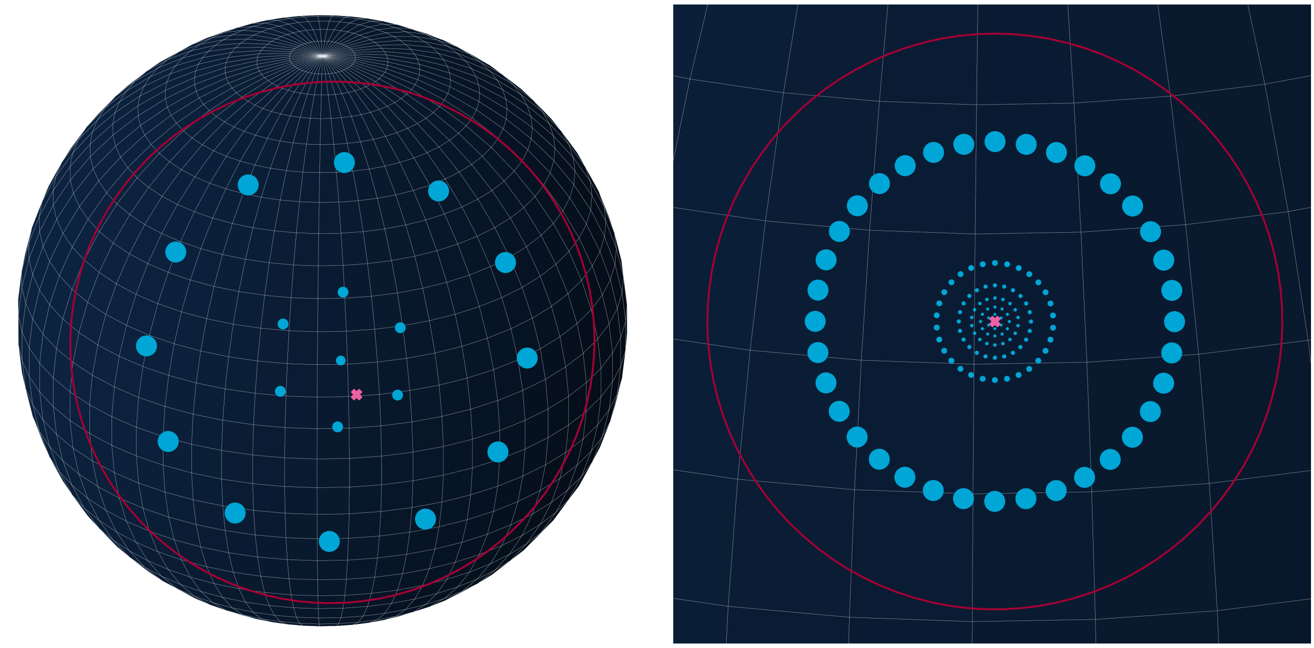

**(a)** High altitude: $h = 1500$ km, 2 rings, angular diameter of cap = 115°. **(b)** Low altitude: $h = 50$ km, 6 rings, angular diameter of cap = 27°.

**Figure 2.** Panels generated with Knocke's algorithm for the Moon, which has a mean radius of 1737 km. The spacecraft (✖) sees a spherical cap (—), which contains rings of panels and is larger at higher altitudes $h$. Panel centers (●) are scaled proportionally to the panel area. The panels have equal projected, attenuated areas and are therefore concentrated around the subsatellite point. The scenario in b corresponds to LRO's orbit and the paneling used in this paper.

the edge of the visible cap. These patterns are a result of the equal projected, attenuated areas.

*Paneled sources: Radiosity models* The emitted and reflected fluxes of each panel are described by radiosity models. The irradiance at the target position can then be derived from the panel radiosity. Both radiosity and irradiance commonly have units of $\mathrm{W/m^2}$. Each panel can have one or more radiosity models, usually one for albedo radiation and one for thermal radiation. We present three such models.

The albedo radiosity model accounts for diffuse Lambertian reflection of solar radiation. It implements the specular–diffuse BRDF from Equation (3) with $C_s = 0$ and the albedo value $C_d = a$ at the panel center. The albedo radiosity of a panel is [22]

$$J_{\text{albedo}} = a \left(\cos\theta_i\right)_+ E_s, \tag{9}$$

where $E_s$ is the incoming solar irradiance at the panel (e.g., as found from Equation (6)) and the solar incidence angle $\theta_i$ is defined in Figure 1. The operator $(\cdot)_+$ restricts the input to positive values or zero otherwise. This ensures that no radiation incident on the backside is reflected.

The delayed thermal radiosity model assumes that absorbed radiation is emitted independently of incident solar radiation and the radiosity is thus not a function of $\theta_i$. The only spatial variations arise from emissivity differences. The emissivity $e$ of a surface is the ratio of the actual radiosity to the ideal black body radiosity. The delay arises from the planet's large thermal inertia. The delayed thermal radiosity of a panel is [22]

$$J_{\text{thermal}} = e\frac{E_s}{4}, \tag{10}$$

where $e$ is the emissivity of the panel, evaluated at its center. The factor 1/4 is the ratio of the absorbing area (a circle) to emitting area (a sphere). The albedo and delayed thermal model were originally used by Knocke *et al.* for Earth emissions [22].

The angle-based thermal radiosity model is more appropriate than the delayed model if the surface experiences significant diurnal cooling and heating. The surface temperature is modeled as a function of the solar incidence angle $\theta_i$ and related to the radiosity through the Stefan–Boltzmann law. The surface temperature is interpolated between the minimum and maximum temperatures, $T_{\text{min}}$ and $T_{\text{max}}$, as [27]

$$T = \max\left(T_{\text{max}}\left(\cos\theta_i\right)_+^{1/4}, T_{\text{min}}\right). \tag{11}$$

These temperatures typically correspond to the nighttime temperature and the temperature at the subsolar point. The angle-based thermal radiosity of a panel is then [27]

$$J_{\text{thermal}} = e\sigma T^4, \tag{12}$$

where $T$ is the surface temperature from Equation (11) at the panel center and $\sigma = 5.670 \times 10^{-8}\,\mathrm{W/(m^2\,K^4)}$ is the Stefan–Boltzmann constant. On the dayside, the radiosity is proportional to $T_{\text{max}}^4 \cos\theta_i$. The maximum radiosity of $e\sigma T_{\text{max}}^4$ is usually larger than the near-constant $eE_s/4$ from Equation (10), but quickly decreases as the panel moves away from the subsolar point (where $\theta_i = 0°$). On the nightside, the thermal radiosity reduces to $e\sigma T_{\text{min}}^4$.

The albedo and thermal radiosity models depend on the distribution of $a$ and $e$ over the planetary surface. The values may be assumed constant but generally vary with longitude, latitude, and time. Particularly for Earth, seasons and weather greatly affect reflectivity and emissivity [28]. Since the Moon lacks seasons, distributions that only vary spatially are sufficient.

To obtain the irradiance at the target due to the panel radiosity, we account for the projected, attenuated area of the source panel and assume that the emissions follow Lambert's cosine law. The irradiance therefore is

$$E = \left( \sum_{J_i \in \mathcal{J}} J_i \right) \frac{\mathrm{d}A \left(\cos \theta_r\right)_+}{\pi \left\| \mathbf{r}_{t/s} \right\|^2}, \tag{13}$$

where $\mathcal{J}$ is the set of radiosities from any of the previous radiosity models. Usually, a panel has the albedo model and one thermal model. Here, the source-to-target vector $\mathbf{r}_{t/s}$ uses the panel center position, not the source body center. The direction $\hat{\mathbf{r}}_{t/s}$ of the corresponding directional irradiance $\mathbf{E} = E\hat{\mathbf{r}}_{t/s}$ is therefore not the same for each panel and thus considers the extent of the source. The radiosities $J_i$ in Equation (13) can be summed since their radiation emanates from the same point, the panel center. Contrarily, the directional irradiances $\mathbf{E}$ can generally not be summed since the their individual directions need to be retained; the reflectance model of the target may be sensitive to the incoming direction of each ray. Therefore, a set of directional radiances $\mathcal{E}$ is handed to the RP target model for acceleration calculations.

### 2.4 Radiation pressure targets

A RP target is a body that is accelerated by RP. The target model governs how the incident irradiances from point sources and extended sources accelerate the target body.

*Cannonball target* In its simplest form, a target can be modeled as an isotropic sphere, also referred to as a cannonball. This sphere is characterized by a cross-sectional area $A_c$ (independent of orientation), radiation pressure coefficient $C_r$ (incorporating reflectivity and absorption coefficients), and mass $m$. Due to its isotropy, any lateral components cancel and the net acceleration is always along the source-to-target vector. The RP acceleration of a cannonball target is [1]

$$\mathbf{a} = C_r \frac{A_c}{m} \sum_{\mathbf{E}_j \in \mathcal{E}} \frac{\mathbf{E}_j}{c}, \tag{14}$$

where the sum is vectorial and $\sum \mathbf{E}_j / c$ is the total RP as described in Section 2.1. $\mathcal{E}$ is the set of directional irradiances from any number of sources, both point (Equation (6)) and paneled (Equation (13)). The dependence on the area-to-mass ratio $A_c/m$ is similar to drag accelerations. While the cannonball model cannot account for complex geometry, it is often used in orbit determination with $C_r$ as estimated variable. Ray tracing of a detailed model can help to establish the evolution of $A_c$ and $C_r$ [29].

*Paneled target* In reality, the cross-section and optical properties of a spacecraft change with orientation and incident direction. This effect is particularly noticeable for solar panels, which are large and usually track the Sun. To account for the geometry and differences in materials, a spacecraft can be represented as a collection of $n$ panels. Each panel is characterized by its area, surface normal, and reflectance distribution. The position would only be relevant for rotational but not for linear accelerations. In the case of moving parts, the surface normal may change over time. The reflectance distribution can be given as generic BRDF, but is often a specular–diffuse BRDF. The RP acceleration of a paneled target is [30]

$$\mathbf{a} = \frac{1}{m} \sum_{\mathbf{E}_j \in \mathcal{E}} \left( \frac{\|\mathbf{E}_j\|}{c} \sum_{k=1}^{n} A_k \left(\cos \theta_{i,k}\right)_+ \mathbf{R}_k \right), \tag{15}$$

where the indices $j$ and $k$ denote the (sub-)source and the target panel, respectively. $A_k$ is the area of the $k$-th panel. $\theta_{i,k}$ is the incidence angle of $\mathbf{E}_j$ onto the $k$-th panel. $\mathbf{R}_k$ is the reaction vector as defined by Equations (2), (4) or (5), depending on the BRDF. The reaction vector is a function of the panel surface normal $\mathbf{N}$ and the target-to-source direction $\mathbf{L} = -\hat{\mathbf{E}}_j$. Therefore, the inner sum has to be evaluated for each directional irradiance $\mathbf{E}_j$ of the outer sum. However, $\mathbf{E}_j$ itself is only calculated once for all panels at the target center to avoid quadratic computational complexity. In general, the resulting acceleration is not along the source-to-target direction as for the cannonball.

Extensions for the paneled target model exist. The model described above does not account for self-shadowing, which occurs when one ray would intersect two panels. This effectively reduces the area of the shadowed panel, an effect that can be significant for complex spacecraft geometries [31]. Polygon intersections enable simple calculation of the effective area [31]. Ray tracing is more involved but can also account for multiple reflections between target panels [32].

Another extension is the radiation pressure due to the thermal radiation of the spacecraft itself. Instantaneous reradiation, as modeled by Equation (5) for the case of thermodynamic equilibrium, is a simple variant of this effect. In reality, panels heat up and cool down (particularly during eclipses) through radiation, conduction, and internal heat production. Advanced models, therefore, calculate the temperature of each panel. Such models range from a simple heat balance [16] to finite element models [25]. However, a lack of knowledge of the thermal properties may restrict the applicability. For the sake of simplicity, neither self-shadowing nor exact thermal radiation pressure of the spacecraft were considered in this paper.

### 2.5 Occultation

All previous models assume that the line of sight between the the source and the target is unobstructed. However, occultation is a common astronomical phenomenon: a low-altitude spacecraft may be in the planet's shadow for more than a third of its orbit, and partial or full lunar eclipses can occur multiple times per year. We present two occultation models.

*Shadow function* The shadow function $\nu$ describes the fraction of light received from a spherical source in the presence of an occulting spherical body. The geometry of the conical occultation model is shown in Figure 3. In the umbra, the source is fully occulted and the observer does not receive any radiation ($\nu = 0$), a state referred to as total eclipse. In the penumbra, the observer can see part of the source ($0 < \nu < 1$). Only outside the shadow region does the

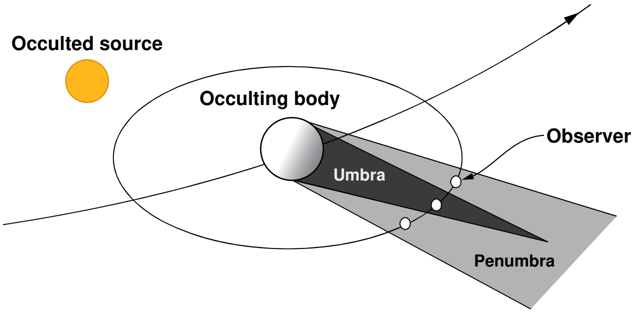


**Figure 3.** Conical occultation model for spherical sources and occulting bodies. The observer is partially illuminated in the penumbra but fully shadowed in the umbra. Adapted from [33].

observer receive the full radiation ($\nu = 1$). In the case of a lunar eclipse, Earth occults the Sun and casts a shadow onto the Moon such that there is no lunar albedo radiation. On the nightside of a planet, the planet itself occults the Sun.

With the models described in Sections 2.3 and 2.4, the shadow function needs to be considered for radiation from a point source, both when directly incident on the target and when used as solar radiation for albedo radiosity. The extent of the source and occulting bodies needs to be known for shadow function calculations, even in the case of point sources. A derivation of the commonly used conical model for $\nu$ is presented by Montenbruck and Gill [1].

The conical model can only account for one occulting body. In the case of multiple occulting bodies, shadows might overlap and the product of their shadow functions would underestimate the actual received fraction. Knowledge of the shadow intersection would be required to avoid this. Zhang *et al.* derived a model for two occulting bodies [34].

More involved shadow models exist that improve the prediction of the penumbra passage. These models can consider planetary oblateness and atmospheric effects like absorption, scattering, and refraction [35]. Other models can account for topography by combining a paneled Sun model with a topography map [9]. These modifications usually prolong the penumbra duration. However, only single occultations from the simple conical model were considered in this paper.

*Point-to-point visibility* For source panels represented by their center point, the shadow function becomes binary: either there is a line of sight between the panel center and the target or there is not. Such point-to-point visibility with a spherical occulting body is easily modeled geometrically. A derivation is given by Vallado and Wertz [33]. Multiple occultations are supported in this occultation model by the logical conjunction of the individual visibilities.

## 3 Radiation pressure modeling for LRO

After describing RP modeling in general, we now present models that are specific to LRO. This includes the source models for lunar radiation and the target models. We also elaborate LRO's orbit geometry and the simulation setup.

### 3.1 Lunar albedo radiation

The Moon is a major source of radiation in LRO's orbit, with lunar irradiance magnitudes approaching the Sun's. Therefore, albedo and thermal radiation due to the Moon should be considered. While the lunar albedo is only $40\,\%$ of Earth's albedo [28], albedo radiation due to the Moon is still substantial, particularly over the subsolar point [6]. Lunar albedo varies significantly with geology: the highlands (mean $a = 0.16$, maximum $a = 0.25$) are much more reflective than the maria (mean $a = 0.07$, minimum $a = 0.05$) due to their respective regolith composition [37–39]. The mosaic of calibrated albedo imagery from Clementine in Figure 4a clearly shows the differences between highlands and maria. The mean of 0.12 agrees with other literature [37], and most of the lunar surface has an albedo below 0.20. Higher values are only found at the poles, where the imagery represents topographic shading rather than actual albedo [40]. Note that lunar reflectivity increases with wavelength [41]; the mosaic is for the albedo of light at $750\,\mathrm{nm}$ wavelength, which is slightly longer than the average solar wavelength. Solar radiation has the most energy within the $300\,\mathrm{nm}$ to $2400\,\mathrm{nm}$ band, but the spectrum peaks at around $470\,\mathrm{nm}$ [42].

Floberghagen *et al.*'s $15 \times 15$ spherical harmonics expansion called Delft Lunar Albedo Model 1 (DLAM-1) [6] is often used to represent the spatial albedo variability in lunar RP models. DLAM-1 was fitted from Clementine imagery and was designed to work with Knocke's albedo model for dynamic paneling (Equation (9)). Due to the nature of spherical harmonics, the model cannot resolve features smaller than $12°$ ($360\,\mathrm{km}$ at the equator). The expansion is shown in Figure 4b. DLAM-1 was derived from 750 nm imagery, but we scale the original values by $1/1.3$ to account for the reduced reflectivity at the average solar solar wavelength. This factor was proposed by Vasavada *et al.* [37]. However, even with the correction, the mean albedo of the expansion of 0.15 is $25\,\%$ above the commonly accepted mean of 0.12. Particularly the highlands appear excessively bright. This is possibly due to a different calibration of the imagery that DLAM-1 is based on compared to the mosaic from Figure 4a. Indeed, Clementine is known to overestimate albedo due to bad calibration [41]. Notwithstanding the difference in magnitude, the maria and highlands can be clearly registered.

Despite the shortcomings of DLAM-1, spherical harmonics are convenient: they are smooth, differentiable, do not require interpolation like a gridded map, and can easily be truncated to trade detail for computational efficiency. Therefore, we used DLAM-1 in this paper but consider that the magnitude may be overestimated by $25\,\%$ during the analysis of results. We also compare results for the location-dependent DLAM-1 with those for a constant value, which should be more computationally efficient. As a single representative albedo, we choose the mean of 0.15 instead of 0.12 to facilitate comparison. Note that the spatial variability described above suggests that a single albedo value cannot accurately represent lunar reflectivity.

Albedo radiation assumes ideal, diffuse Lambertian reflectance, which decreases with the cosine of the viewing angle. This assumption is especially appropriate for Earth, for which purely specular radiosity only amounts to $10\,\%$ of the purely diffuse radiosity [22]. However, this is not the case for the Moon: the opposition effect increases the reflectance at small phase angles (when the source is behind the observer, see Figure 3) much more than would be expected from a

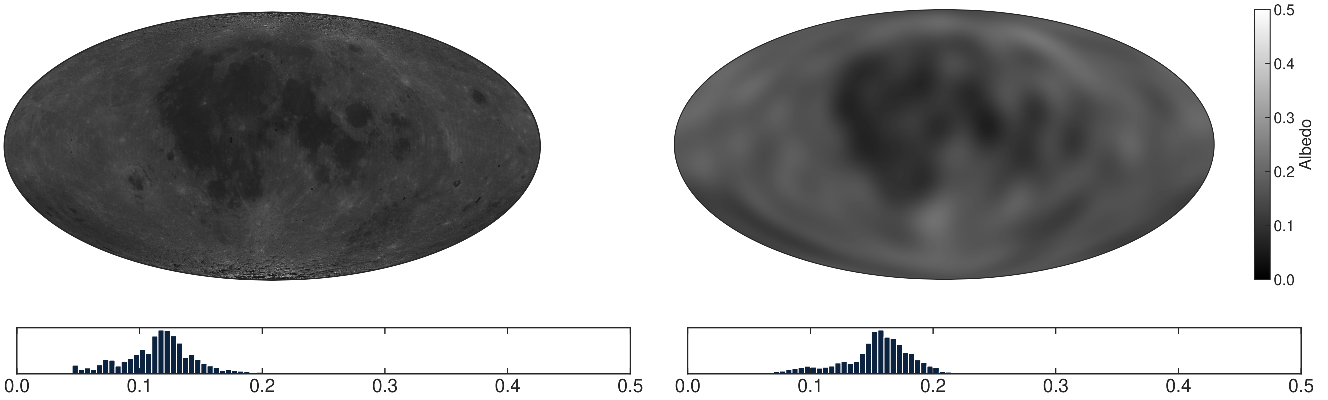


**(a)** Mosaic (mean = 0.12, minimum = 0.05, 99th percentile = 0.29) [36] **(b)** DLAM-1 (mean = 0.15, minimum = 0.06, 99th percentile = 0.21)

**Figure 4.** Lunar albedo distributions from Clementine. Both the mosaic and DLAM-1 are based on 750 nm reflectivity, but DLAM-1 has been corrected to the average solar wavelength. Note that the maximum of the albedo scale here is 0.5 instead of 1.0 to increase contrast; in reality, the Moon appears half as bright.

cosine law. In fact, the brightness increases more than $40\,\%$ between phase angles of $4°$ and $0°$ [43]. This is primarily caused by shadow hiding. To account for the non-diffuse reflectance of the lunar surface, the Hapke BRDF was developed [44]. This BRDF is an empirical relation based on nine parameters that control, among other properties, the strength and directionality of the opposition effect. Near-global maps for these parameters have been fitted from LRO observations and could be used for a radiosity model [39]. For RP acceleration modeling, the opposition effect is only of concern when the target is above the subsolar point, which requires the Sun to be in the orbital plane. For LRO, this only occurs twice a year for a few days, and even then only for a small fraction of the orbit. Therefore, we neglected the opposition effect in this paper.

### 3.2 Lunar thermal radiation

Lunar surface temperatures and the associated thermal radiation undergo a significant diurnal cycle. Daytime and nighttime temperatures can differ by up to $290\,\mathrm{K}$. The surface heats rapidly after sunrise, cools at about the same rate after local noon, then slower during the night [37]. There are small seasonal changes, with noon temperatures differing by $6\,\mathrm{K}$ between lunar aphelion and perihelion [23]. The large diurnal variability renders Knocke's delayed thermal model (Equation (10)), which yields a constant radiosity throughout the day, unsuitable for the Moon.

Diurnal variability is represented well by the angle-based thermal model (Equation (12)). We parametrize the model with the equatorial temperatures just before sunrise ($T_{\mathrm{min}} = 95\,\mathrm{K}$) and at local noon ($T_{\mathrm{max}} = 385\,\mathrm{K}$) [37]. The model transitions to the nighttime temperature when the incidence angle $\theta_i \geq 89.8°$. Our temperatures span a slightly larger range than those of Lemoine *et al.* ($T_{\mathrm{min}} = 100\,\mathrm{K}, T_{\mathrm{max}} = 375\,\mathrm{K}$), who initially proposed the angle-based model. However, they agree with those used by Park *et al.* [45]. Note that Park *et al.*'s model is identical to ours except for a factor $1/4$ in the radiosity, which is incorrect.

While the albedo varies with location (see Section 3.1), the lunar emissivity and other thermophysical properties are remarkably uniform [38]. This means that constant emissivity is a fair assumption. We used a value of $e = 0.95$, which is the broadband daytime emissivity, although it decreases to 0.90 during the night [46]. However, we assumed the constant daytime emissivity at all times.

The thermal surface radiosity $J_{\mathrm{thermal}}$ from the angle-based model with the aforementioned parameters is shown in Figure 5. The radiosity decreases with the cosine of the incidence angle and approaches negligible emissions of $6\,\mathrm{W/m^2}$ at nighttime. The maximum radiosity, which occurs below the subsolar point (i.e., at local noon at the equator), is $1250\,\mathrm{W/m^2}$. This peak value agrees with those used to design LRO's thermal control subsystem [2]. The only effect that is not captured is the slow cooling by about $25\,\mathrm{K}$ between sunset and sunrise [37], which introduces a slight asymmetry; constant pre-sunrise temperatures are used throughout the night. We also do not model seasonal variations of surface temperature.

### 3.3 Paneling of the Moon

The Moon needs to be discretized to evaluate the albedo and thermal radiation numerically. LRO's low altitude compared to the lunar radius prohibits any static paneling, which would

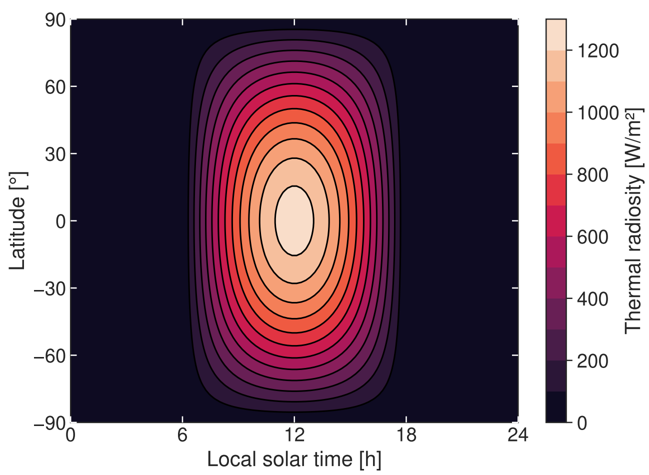


**Figure 5.** Map of lunar thermal emissions from the angle-based model (Equation (12)), peaking at $1250\,\mathrm{W/m^2}$. The emissivity is 0.95 and surface temperatures range between 95 K and 385 K, depending on the subsolar angle.

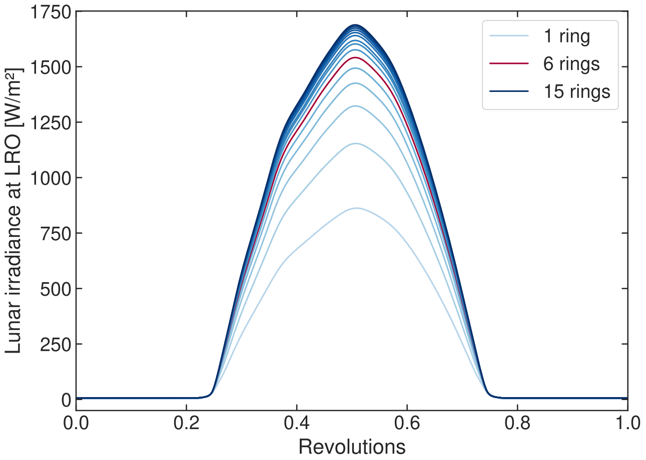


**Figure 6.** Convergence of lunar irradiance received by LRO for increasing number of rings. Each ring contains six more panels than the previous one. Six rings (—) are sufficient for an error of less than 10 % with respect to the converged solution.

result in a large number of invisible panels. Therefore, we used Knocke's dynamic paneling method (Section 2.3).

Selecting the number of rings is a trade-off between fidelity and computational efficiency. To determine the lowest number of rings that can still represent lunar radiation with sufficient accuracy, we investigated the convergence behavior. Figure 6 shows the albedo and thermal irradiance received by LRO for an increasing number of rings. As suggested by Knocke *et al.*, each ring contains six more panels than the previous one. For 13 rings and more, the peak irradiance is within 1 % of $1690\,\mathrm{W/m^2}$. For six rings, the irradiance peaks at $1540\,\mathrm{W/m^2}$, which is within 10 % of the converged solution. The results are similar for constant and DLAM-1 albedo.

We choose six rings comprising 127 panels in total as sufficiently accurate (cf. Figure 2b). This is one ring (or 36 panels) more than used by others. Floberghagen *et al.* suggested five rings for Lunar Prospector, which has twice the orbital altitude of LRO and thus needs fewer rings (Knocke *et al.* used only two rings for a much higher altitude relative to the planetary radius). Five rings were also used for LRO's precision orbit determination [10]. We chose one ring more to keep the error due to paneling below 10 %. More panels may be required in case of a higher-resolution albedo distribution.

### 3.4 LRO target

LRO comprises a cubical bus with a large solar array and a protruding high gain antenna (Figure 7). Different sides are presented to solar and lunar radiation. The solar array can be gimbaled partially about the Y and Z axes such that it can track the Sun when it is within LRO's orbit plane; when not, the solar array is fixed at a 45° angle with the -Y bus side. The antenna points toward Earth whenever it is visible [9]. Both of this leads to large variations in cross-section over time.

LRO can be modeled as a paneled target (Equation (15)) to account for this variability. Table 1 summarizes the panels. There are six panels for the bus, with surface normals along the positive and negative axes of the LRO bus frame (cf. Figure 7). The solar array and high gain antenna are modeled separately, again with front and back panels. The solar array

**Table 1.** Panels for LRO target model from Smith *et al.* [11]. The coefficients are for absorptivity and specular/diffuse reflectivity. The solar array is by far the largest surface, followed by the Z-facing panels. SA: solar array; HGA: high gain antenna.

| Panel | $C_a$ | $C_s$ | $C_d$ | A [$\mathrm{m^2}$] | Tracking |
|---|---|---|---|---|---|
| +X | 0.49 | 0.29 | 0.22 | 2.82 | |
| -X | 0.42 | 0.39 | 0.19 | 2.82 | |
| +Y | 0.45 | 0.32 | 0.23 | 3.69 | |
| -Y | 0.50 | 0.32 | 0.18 | 3.69 | |
| +Z | 0.50 | 0.32 | 0.18 | 5.14 | |
| -Z | 0.28 | 0.54 | 0.18 | 5.14 | |
| +SA | 0.90 | 0.05 | 0.05 | 11.00 | +Sun or fixed |
| -SA | 0.50 | 0.30 | 0.20 | 11.00 | -Sun or fixed |
| +HGA | 0.54 | 0.18 | 0.28 | 1.00 | +Earth |
| -HGA | 0.93 | 0.02 | 0.05 | 1.00 | -Earth |

is almost as large as all other panels combined. Panels for the solar array and high gain antenna track the Sun and Earth or have a fixed orientation, as described above. Definitive attitudes of actuated panels are also available but were not used.

We also model LRO as a cannonball (Equation (14)), a model which is often used for orbit determination. Finding a single equivalent cross-section area $A_c$ and coefficient $C_r$ that hold at all times is virtually impossible [33]. Different values for LRO exist in literature: Bauer *et al.* used $A_c = 10\,\mathrm{m^2}$ and $C_r = 1.2$ [12], while Nicholson *et al.* used $A_c = 14\,\mathrm{m^2}$ and $C_r = 1.0$ [10]. Their acceleration should differ by about 15 %. We choose the latter since it is used for operational orbit estimation of LRO.

To complete the target model, the mass is required to transform forces into accelerations. LRO performed monthly station-keeping maneuvers during its science mission phase, which reduced the initial mass after science orbit insertion from 1272 kg to 1087 kg (Figure 8). With every maneuver, 6.3 kg of propellant are expelled [48]. This increases

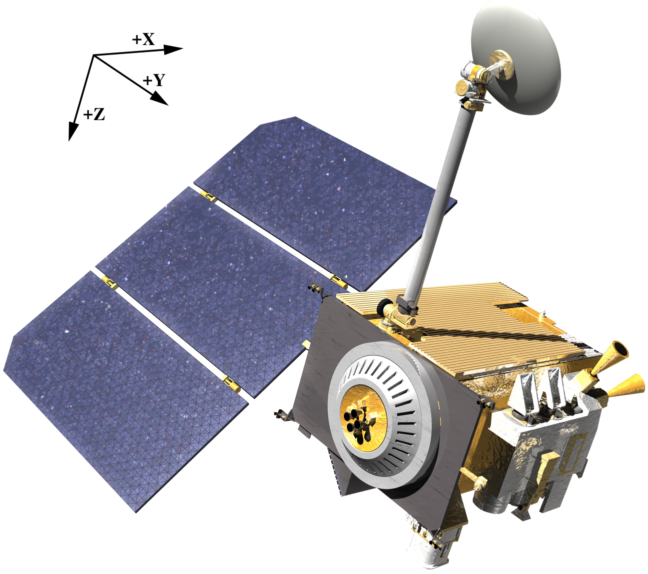


**Figure 7.** Rendering of LRO [47] with bus frame definition. The X axis is along the velocity vector, the +Y axis is away from the Sun, and the +Z axis is in the nadir direction [2].

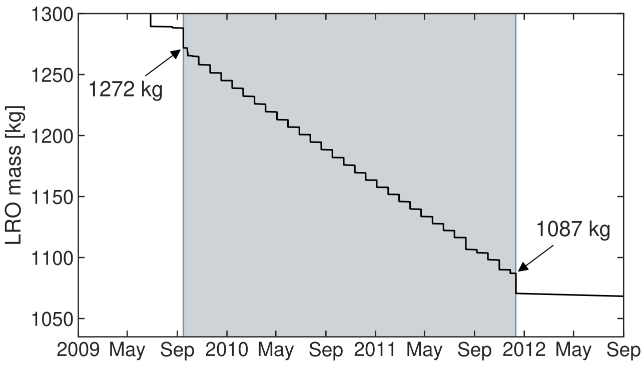


**Figure 8.** Mass evolution of LRO over the science mission phase (■). LRO expelled 185 kg of propellant for station keeping between 15 September 2009 and 11 December 2011.

accelerations by $15\,\%$ over the course of 21 months. To facilitate comparison and obtain worst-case results, we used the end-of-mission mass of $1087\,\mathrm{kg}$ in this paper, independently of the actual arc.

### 3.5 LRO orbit geometry

LRO's polar science mission orbit has a period of $113\,\mathrm{min}$ and a low altitude of $50 \pm 15\,\mathrm{km}$. The difference between periselene and aposelene is mostly due to a slight eccentricity, but also an equatorial radius that is $2\,\mathrm{km}$ larger than the polar radius. The altitude variation affects the lunar irradiance received by LRO.

The visibility of the Sun is determined by the beta angle $\beta$, which is the angle between the orbital plane and the Moon-to-Sun vector. It is zero when the Sun is within the plane and $\pm 90°$ when the orbit normal points toward or away from the Sun. Since LRO's orbit is polar, it undergoes all $\beta$ within a year. For $\beta = 0°$, LRO is moving straight toward and away from the Sun above the poles, experiences the maximum eclipse duration on the nightside, and passes over the subsolar point. For $\beta = 90°$, LRO is in full view of the Sun throughout the orbit and does not pass over hot or well-illuminated lunar regions. Far large $\beta$, LRO's solar array has a fixed orientation as mentioned in Section 3.4. Since the solar array then covers most of the -Y side, self-shadowing of up to $40\,\%$ of the total cross-section can occur for solar radiation [9]. Self-shadowing is no issue for small $\beta$. In this paper, we neglected self-shadowing, which was shown to only have a minor impact in most cases [5, 49].

Since the effect of RP varies greatly with $\beta$, we investigated two contrasting arcs, which are summarized in Table 2. In June, Moon is at aphelion and no eclipses occur since LRO is continuously illuminated at $\beta \approx 90°$. In September, $\beta$ is just below $0°$ so LRO experiences the maximum solar eclipse duration of $48\,\mathrm{min}$. No lunar eclipses occur during any of the arcs. Both arcs have a length of 2.5 days, which is also used for orbit determination of LRO [8, 10]. Choosing the same length ensures our results are a relevant indicator of force modeling error during orbit determination.

**Table 2.** Orbit geometry for selected arcs over 2.5 days. The June arc has permanent illumination, the September arc has the maximum eclipse duration.

| | **28 June 2010** | **26 Sept. 2011** |
|---|---|---|
| **Start time (UTC)** | 15:00:00 | 18:00:00 |
| **Beta angle $\beta$ [°]** | 88.8 to 88.9 | $-1.7$ to $-3.6$ |
| **Sun distance [au]** | 1.019 | 1.000 |
| **Eclipse time [min]** | 0 | 48 |
| **Solar array** | Fixed (45° to -Y) | Tracks Sun |

### 3.6 Simulation setup

A range of simulations with varying models is necessary to determine the orbital effects of RP modeling choices. However, a common setup, presented in Table 3, enables comparison. Some items should be clarified:

- Gravity due to Jupiter and Venus is neglected since it is 7 orders of magnitude lower than Earth's.
- Albedo and thermal radiation due to Earth is neglected since it is 3 orders of magnitude lower than the Moon's.
- The occultation of solar radiation by the Moon follows a simple conical model. Time spent in sunlight can be overestimated by up to $480\,\mathrm{s}$ for large $\beta$ if the topography is ignored [9].
- No lunar eclipses occur over the two simulation arcs, therefore occultation by Earth can be ignored.
- Good accuracy can be achieved with integration step sizes as high as $15\,\mathrm{s}$ [9]. We use $5\,\mathrm{s}$, which is used for operational orbit determination [10].
- While the Moon has a difference between polar and equatorial radius of $2.1\,\mathrm{km}$ due to flattening, a perfect sphere will be assumed here to simplify paneling and occultation.
- The Moon Mean Earth/Polar Axis frame is recommended for use with LRO [52].
- LRO SPICE kernels containing ephemerides (SPK) and orientation (CK) are available online.

## 4 Results

We analyzed the short-term effects of RP by examining accelerations and the position at the end of the 2.5-day arc. While the position is ultimately relevant for precise orbit determination, studying the accelerations in different scenarios and along the orbit can explain the cause of position changes. Additionally, the accelerations underscore differences between models of varying complexity.

To compare two accelerations over time, we used the root mean square error (RMSE), which is defined as

$$\mathrm{RMSE}(x, y) = \sqrt{\frac{1}{n}\sum_{i=1}^{n}(x_i - y_i)^2}. \tag{16}$$

The RMSE describes the difference between two scalar time series $x_i, y_i$ and gives more weight to large deviations. These time series can be the magnitude of accelerations or individual components. The relative root mean square error (rRMSE) is defined as

$$\mathrm{rRMSE}(x, y) = \sqrt{\frac{\sum_{i=1}^{n}(x_i - y_i)^2}{\sum_{i=1}^{n} y_i^2}} \tag{17}$$

and is useful to compare differences across orders of magnitude.

**Table 3.** Common setup for all simulations. Gravity and radiation pressure are the only force models.

| | | |
|---|---|---|
| **Planetary bodies** | | |
| Planetary ephemerides | DE 421 [50] | |
| Moon ellipsoid | Sphere of radius 1737.4 km [51] (no flattening) | |
| Moon reference frame | Mean Earth/Polar Axis [52] | |
| **Force models** | | |
| Moon gravity | GRGM1200L [53] (truncated to $100 \times 100$) | |
| Earth + Sun gravity | Central | |
| Solar radiation | Isotropic point source ($L = 3.828 \times 10^{26}$ W [19]) | Equation (6) |
| | Occulted by Moon | |
| Lunar radiation | Paneled source with 6 rings of 6, 12, 18, 24, 30, and 36 panels | |
| | Albedo: Constant ($a = 0.150$) or DLAM-1 | Equation (9) |
| | Thermal: Angle-based ($e = 0.95$, $T_{\text{min}} = 95$ K, $T_{\text{max}} = 385$ K) | Equation (12) |
| RP target | Cannonball ($A_c = 14\,\text{m}^2$, $C_r = 1.0$) or Paneled (see Table 1) | Equations (14) and (15) |
| | Paneled model with or without instantaneous reradiation | Equations (4) and (5) |
| | Mass: 1087.0 kg (end of science mission) | |
| | Orientation: LRO_SC_BUS frame from SPICE CK | |
| **Simulation settings** | | |
| Software | TU Delft Astrodynamics Toolbox (Tudat) 2.12.1.dev19 | |
| Propagation frame | ECLIPJ2000 | |
| Propagation method | Cowell | |
| Integration method | Runge–Kutta–Fehlberg 7(8) | |
| Step size | 5 s (fixed) | |
| Arc length | 2.5 days (31.9 revolutions) | |
| Initial state | Cartesian state from SPICE SPK (lrorg_*) | |

While the simulation evaluates accelerations in a global frame, the effect of accelerations on the orbit is best analyzed in a spacecraft-fixed coordinate system that is aligned with the orbital track. The RSW coordinate system is one such system, defined by the unit vectors [33]

$$\mathbf{R} = \frac{\mathbf{r}}{\|\mathbf{r}\|}, \quad \mathbf{W} = \frac{\mathbf{r} \times \mathbf{v}}{\|\mathbf{r} \times \mathbf{v}\|}, \quad \text{and} \quad \mathbf{S} = \mathbf{W} \times \mathbf{R}. \tag{18}$$

The radial component $\mathbf{R}$ is aligned with the planetocentric position vector $\mathbf{r}$. The cross-track component $\mathbf{W}$ is aligned with the angular momentum vector, or orbit plane normal, and involves the linear velocity $\mathbf{v}$. The along-track component $\mathbf{S}$ completes the right-handed coordinate system. Note that $\mathbf{S}$ is generally not perfectly aligned with the velocity vector, but can be considered so for LRO's approximately circular orbit.

### 4.1 Instantaneous reradiation

First, we investigated the effect of instantaneous reradiation for the paneled target model. This increases the acceleration proportional to each panel's $C_a$ in a direction normal to the panel (cf. Equation (5)).

Figure 9 shows the absolute and relative differences between accelerations without and with instantaneous reradiation. In absolute terms, the radial and along-track components are impacted most for the September arc, while the along-track and cross-track components experience the largest increase for the June arc (for both arcs, up to about $1.9 \times 10^{-8}\,\text{m/s}^2$ RMSE). The relative differences are more uniform (around 40 % rRMSE), but the along-track components of lunar and solar radiation in the June arc increase by 140 % and 570 % rRMSE, respectively. In most cases, only the magnitude of accelerations changes but not the pattern over an orbit.

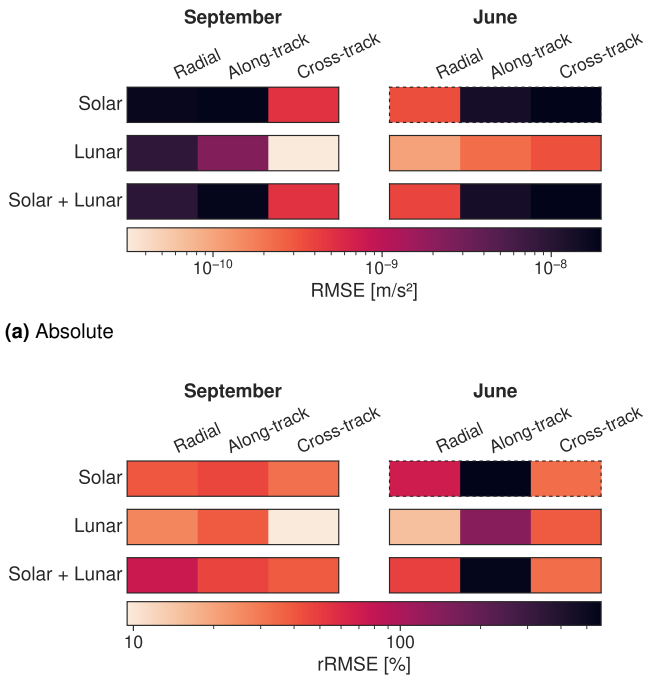


**(a)** Absolute

**(b)** Relative

**Figure 9.** RMS differences of RP accelerations over one orbit with and without instantaneous reradiation. The dashed boxes correspond to Figure 10.

Figure 10 shows the solar radiation of the June arc without and with instantaneous reradiation, the only of our

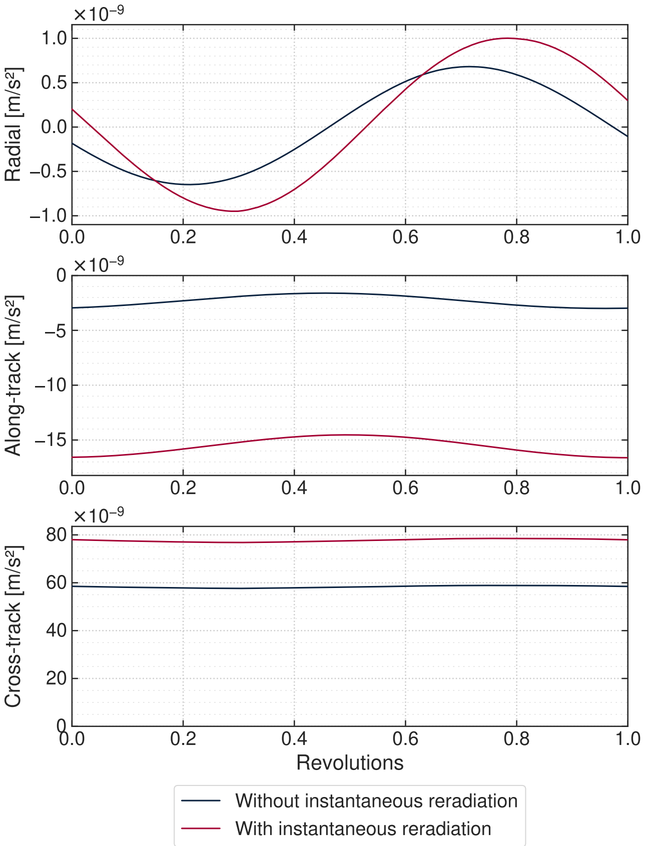


**Figure 10.** Accelerations due to solar radiation without and with instantaneous reradiation over one orbit for the June arc. There is a phase shift in the radial component and the along-track component increased by 570 % RMSE. Lunar contributions and the September arc are not significantly affected in shape.

simulations for which the pattern changed significantly. The phase of the radial acceleration is shifted by about $10\,\%$ of the orbital period, which is not the case for the other two components or the acceleration due to lunar radiation. The solar acceleration of the June arc also had the largest relative change in along-track component as described above (highlighted in Figure 9). This change manifests as a constant offset of about $-13 \times 10^{-9}\,\mathrm{m/s^2}$.

The large changes seen in some cases are mostly due to the +SA panel, which is highly absorptive ($C_a = 0.90$) and large ($A = 11.00\,\mathrm{m^2}$). For the June arc, the solar array is angled at $45°$ with equal components in the cross-track and along-track directions The Sun is on the same side as the solar array in the cross-track direction. Without instantaneous reradiation, no panel has a significant contribution to the along-track acceleration, so it is quite small at around $2 \times 10^{-9}\,\mathrm{m/s^2}$. With instantaneous reradiation, each panel, and especially the solar array, exerts an acceleration parallel to its normal, which leads to the along-track increase witnessed for the June arc.

We applied instantaneous reradiation for all of the following simulations since no reradiation due to spacecraft panels is physically unrealistic and the differences in magnitude are significant when instantaneous reradiation is added. More sophisticated thermal models involving conduction and internal heat generation would likely produce more accurate results.

### 4.2 Accelerations

The most direct effect of RP is visible in the accelerations. Therefore, we compare the RP accelerations

- for the September and June arcs,
- due to solar and lunar (albedo + thermal) radiation,
- for the constant and DLAM-1 albedo distributions,
- for the cannonball and paneled targets.

In total, we ran 46 simulations. All accelerations are given in $10^{-9}\,\mathrm{m/s^2}$. Regarding the cannonball and paneled target models, note that their comparative magnitudes are less important since the choice of cannonball parameters is somewhat arbitrary. Instead, we compared their behaviors and how they relate to model assumptions (e.g., symmetry for the cannonball, tracking for the paneled target).

*Solar and lunar radiation* Both solar and lunar radiation are significant but their accelerations may amplify or cancel each other. To compare them, we used a constant albedo model in addition to the thermal model. The accelerations over one orbit are shown in Figure 11. Note that secular variations in orbit geometry can change the magnitude of acceleration components across orbits even within one 2.5-day arc; secular variations are not shown here.

For the June arc (Figure 11a), the spacecraft is in permanent sunlight and the orbit plane normal points toward the Sun because $\beta \approx 90°$. This leads to extremely large, constant cross-track solar accelerations. The paneled model also has along-track solar accelerations due to the solar array as explained in Section 4.1. Interestingly, the radial solar accelerations show the same phase shift between the cannonball and paneled targets as observed without instantaneous reradiation (Section 4.1). This suggests that symmetry, or the lack thereof, is the cause of the phase shift. The magnitude of the total solar acceleration does not change much throughout the year since it is only dependent on the Moon–Sun distance, which is relatively constant at $1\,\mathrm{au}$ (see Table 2).

The lunar accelerations during the June arc are generally small (less than $2\,\%$ of solar) because LRO never passes over well-illuminated regions; half of the lunar source panels that are visible by LRO are on the nightside and therefore rarely contribute. The sinusoidal variations in lunar radiation pressure are mainly caused by the fact that $\beta$ is not exactly $90°$ and LRO's angle to the subsolar point therefore varies by $2°$. Periodic variations in altitude due to the eccentricity itself have a minimal effect since higher altitudes mean larger distances but also a larger visible area of the lunar surface, which roughly cancels. Secular variations in lunar accelerations (not shown) exist and are due to the evolution of eccentricity over the 2.5 days caused by the non-uniform lunar gravity field [2]. The eccentricity ranges from 0.005 to 0.008, which leads to periselene altitudes between $37\,\mathrm{km}$ and $41\,\mathrm{km}$. Such changes in eccentricity lead to larger amplitudes but no mean shift.

For the September arc (Figure 11b), the Sun is occulted for $42\,\%$ of the orbit since $\beta \approx 0°$. The effect of these occultations is evident in solar and lunar radiation, both of which vanish on the nightside. The accelerations are mostly in the radial and along-track directions. This is most clearly explained by the solar accelerations: At $t = 0.2$,

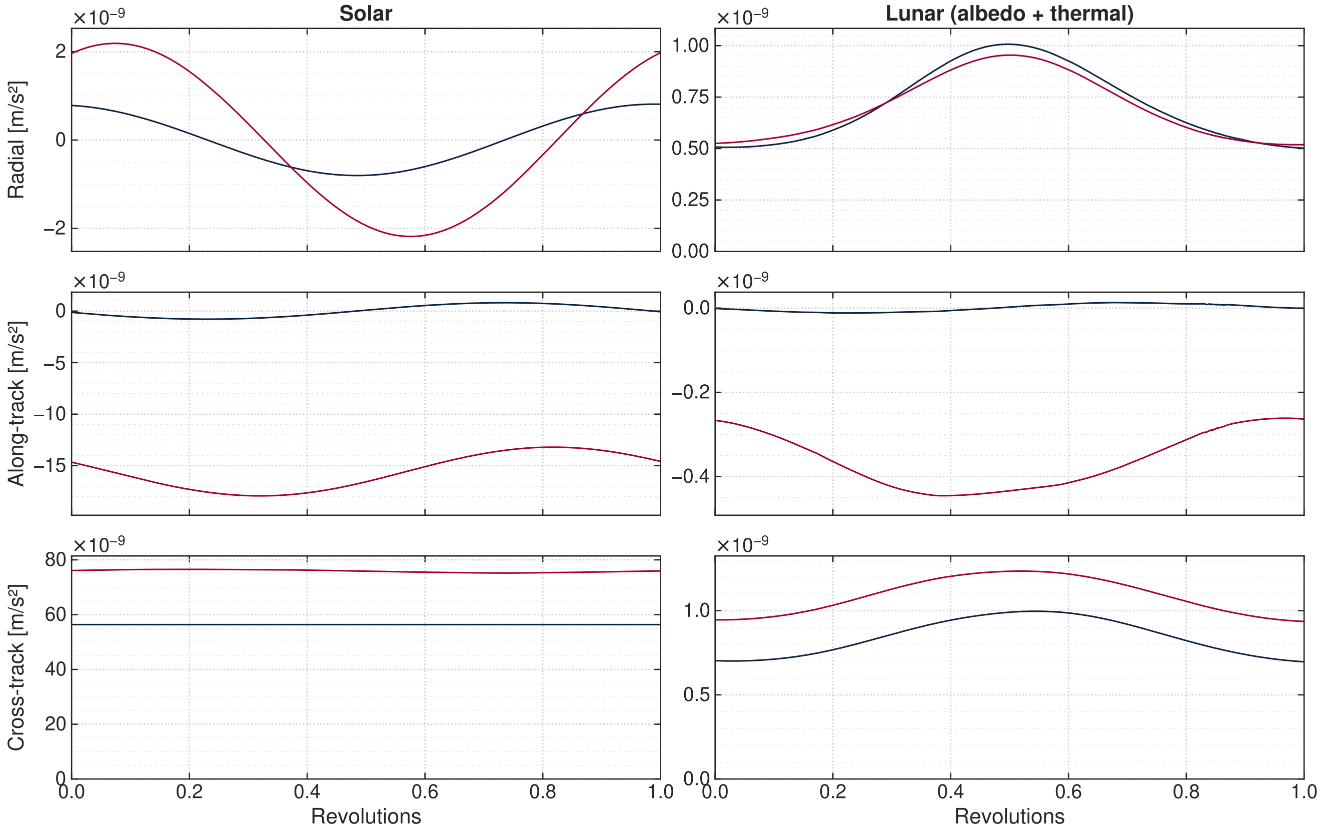


**(a)** June

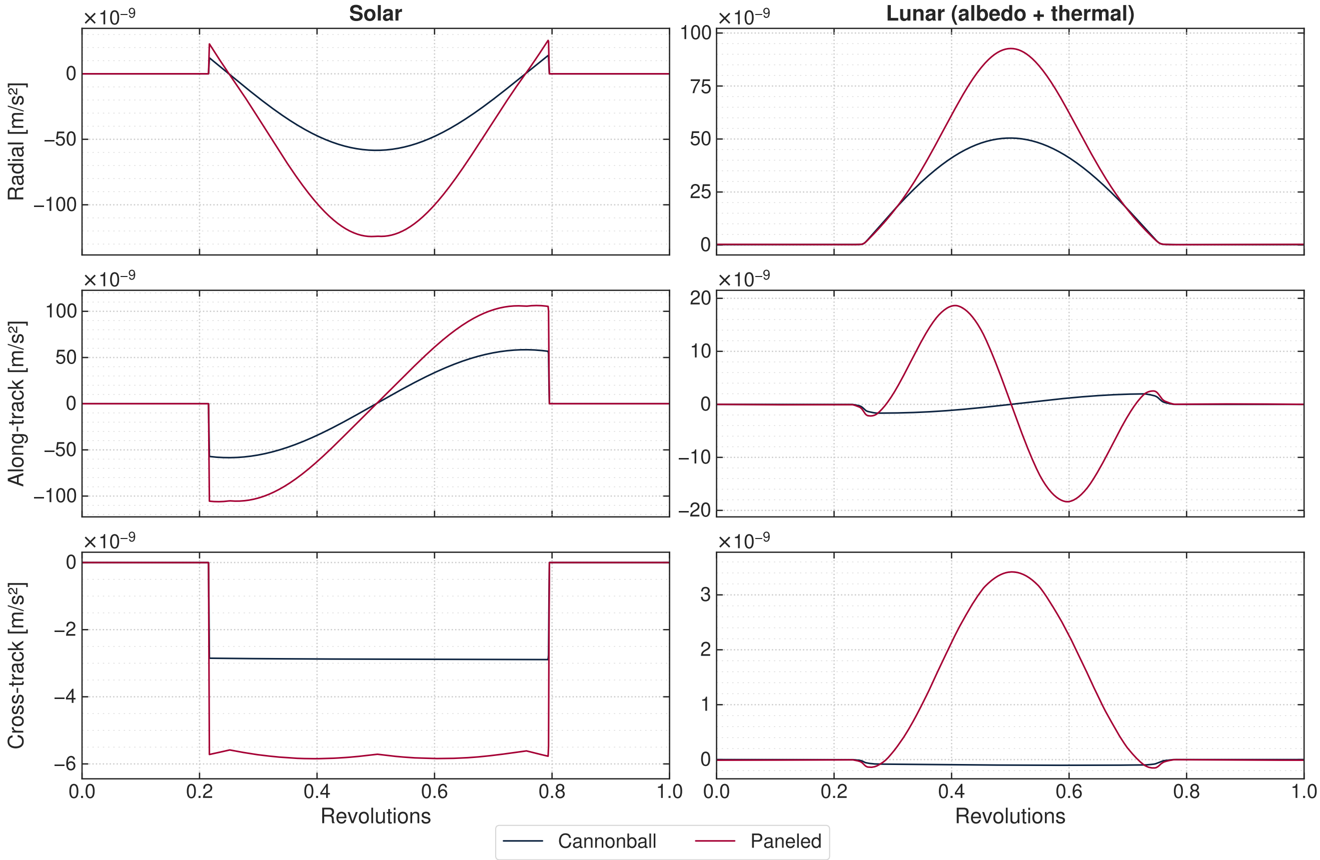


**(b)** September

**Figure 11.** Accelerations due to solar and lunar (thermal + constant albedo) radiation over one orbit. The cannonball and paneled targets differ both in magnitude and pattern of accelerations. Note the different scales of each subplot.

LRO crosses the terminator above the pole and is moving straight toward the Sun; the along-track component is then maximal and negative since the Sun opposes the spacecraft's motion. Continuing the orbit, LRO passes above the subsolar point at $t = 0.5$, leading to a maximal and negative radial component while the along-track component has vanished. Further toward the other pole, LRO passes into the night at $t = 0.8$, where the along-track component accelerates the spacecraft into the direction of motion. During this whole time, the cross-track component is slightly negative because $\beta$ is slightly negative but not zero. If $\beta$ were slightly positive, the cross-track component would be similar but with the sign flipped. In addition to periodic changes, there is a secular change in solar accelerations (not shown) since the already slightly negative $\beta$ continues to decrease: over the 2.5-day arc, the mean of the along-track and cross-track components increase twofold and threefold, respectively. This trend continues until the cross-track component dominates for high $\beta$, as seen for the June arc.

The lunar accelerations during the September arc are much larger than during the June arc because LRO passes right over the subsolar point, which reflects much sunlight and has high thermal emissions. Indeed, the lunar irradiance (up to $1830\,\mathrm{W/m^2}$) is larger than the solar irradiance (up to $1360\,\mathrm{W/m^2}$) above the subsolar point. Still, the lunar acceleration magnitude is $14\,\%$ smaller than the solar acceleration magnitude since lunar panels are distributed azimuthally around the nadir and thus partially cancel while all solar rays are parallel and therefore compound. Another feature of lunar accelerations is the sign opposite to solar accelerations: when passing over the subsolar point, the radial components of solar and lunar accelerations roughly cancel. A similar effect can be seen in the along-track and cross-track components for a paneled target, although the lunar radiation needs some time to build up: The along-track component peaks at a subsolar angle of $33°$, the cross-track component above the subsolar point. The cross-track component increases secularly over the 2.5-day arc, similarly to solar radiation.

Comparing the accelerations of cannonball and paneled targets for both arcs, it is clear that a single $C_r$ cannot capture the complex and changing spacecraft geometry. While the solar accelerations for the September arc are just off by about a constant factor, this is not the case for the June arc or any of the lunar accelerations. In fact, the sign may even be different, particularly for lunar along-track and cross-track accelerations in September. This is likely caused by the solar array tracking the Sun. On smaller scales, the effect of target panels of different sizes and reflective properties becoming illuminated as LRO revolves around the Moon can be seen in the kinks of the solar cross-track accelerations of the September arc.

All accelerations are inversely proportional to the spacecraft's mass. While we chose the end-of-mission mass for all simulations, the begin-of-mission mass is $17\,\%$ higher and all accelerations are thus $15\,\%$ lower (see Section 3.4). This only changes magnitudes, not patterns.

*Lunar albedo and thermal radiation* In the previous subsection, lunar radiation was regarded as the sum of albedo and thermal radiation. In this subsection, we look at the separate contributions and the differences between albedo distributions. The accelerations on a paneled target are shown in Figure 12.

For both arcs and all components, thermal radiation is far larger than albedo radiation (up to sixfold). This is even though the albedo is likely overestimated by $25\,\%$ as described in Section 3.1. In terms of behavior, the thermal radiation and constant albedo radiation are very similar: smooth and dependent on the subsolar angle. However, albedo radiation vanishes in the eclipse region of the September arc. The thermal irradiance at LRO on the nightside is $6\,\mathrm{W/m^2}$, which leads to a small total acceleration of $1 \times 10^{-9}\,\mathrm{m/s^2}$.

The accelerations of the constant and DLAM-1 albedo distributions are of very similar magnitude (in non-zero regions, rRMSE of $14\,\%$ for June and $16\,\%$ for September), although DLAM-1 exihibits irregular variations. The largest difference of $3.7 \times 10^{-9}\,\mathrm{m/s^2}$ occurs in the radial component for the September arc at $t \approx 0.45$. Interestingly, DLAM-1 albedo radiation peaks *before* the subsolar point, whereas the thermal and constant albedo radiation peak above it. This behavior can be explained by Figure 13, which shows the DLAM-1 albedo irradiance along the ground track over a map of the difference between DLAM-1 and the constant albedo. In this figure, the maximum albedo difference also appears before the subsolar point in a region where DLAM-1 has an albedo that is $0.043$ higher or $29\,\%$ more reflective than the constant albedo of $a = 0.150$. All irregular differences between the albedo distributions seen in Figure 12 are explained by this map. Note that larger differences than those seen in June and September may occur for other arcs. However, because the thermal radiation is so much larger, the effect of these differences remains overall limited. Therefore, a constant albedo may be sufficient for most applications.

### 4.3 Change in final position

The goal of orbit determination is to estimate the state, and particularly the position, of a spacecraft over time. Therefore, the difference in position at the end of the arc between models is highly relevant. As mentioned in Section 1, the maximum allowable error for LRO is $50\,\mathrm{m}$ to $100\,\mathrm{m}$ in total position and below $1\,\mathrm{m}$ radially. Since the true position is not known and this paper is rather concerned with relative differences, we used a simulation without solar and lunar radiation as a baseline reference.

The differences in final positions with respect to the baseline simulation are shown in Table 4. The first number is the mean, secular difference over the final orbit (32nd revolution), and the second number gives the amplitude of periodic variations around that mean over the final orbit. Note that the periodic variation is quite large in some cases despite zero secular change.

The June arc shows a large along-track difference (more than $1\,\mathrm{km}$) for the paneled target with solar radiation (**A**). This is likely due to accumulation of the consistently large along-track acceleration of about $-15 \times 10^{-9}\,\mathrm{m/s^2}$. However, this acceleration is of lower magnitude than the constant acceleration of $+47 \times 10^{-9}\,\mathrm{m/s^2}$ expected to result in this position difference, and of the opposite sign. For the cannonball, the along-track accelerations have a zero mean and thus the position difference is also zero. This, again,

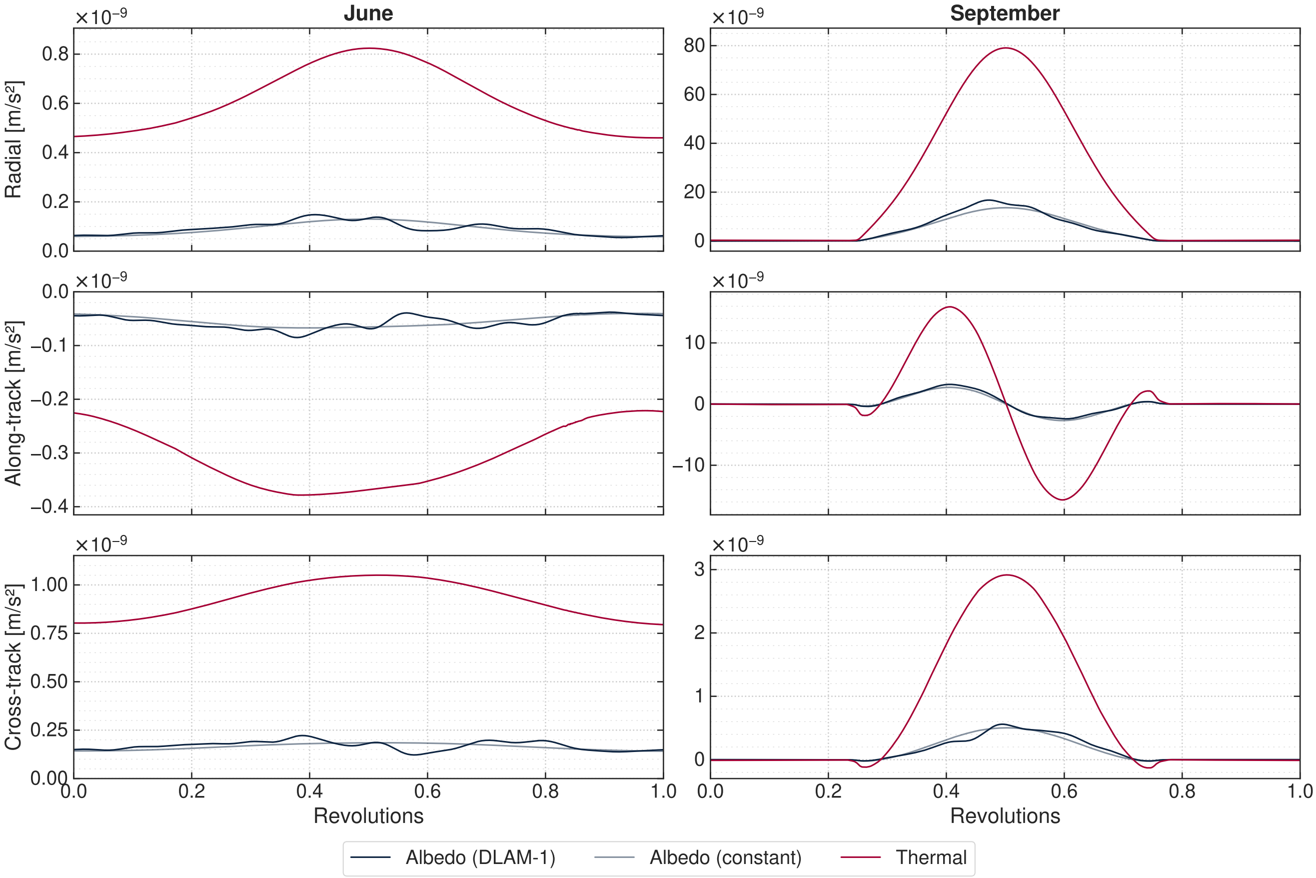


**Figure 12.** Accelerations due to lunar thermal and albedo radiation on a paneled target. Thermal radiation dominates at all times and the difference between constant and DLAM-1 albedo is small. Note the different scales of each subplot.

**Table 4.** Difference of final position in m with respect to the no-RP baseline, given as mean over the final orbit plus/minus periodic variations around that mean. The largest changes are in the along-track position. $\mathbf{A}$: solar only; $\mathbf{B}$: lunar only (thermal + constant albedo); $\mathbf{C}$: lunar only (thermal + DLAM-1 albedo); $\mathbf{D}$: solar + lunar (thermal + DLAM-1 albedo).

| | Cannonball | | | | Paneled | | | |
|---|---|---|---|---|---|---|---|---|
| | Radial | Along-track | Cross-track | RMSE | Radial | Along-track | Cross-track | RMSE |
| **A** | $+0.0 \pm 0.2$ | $-0.5 \pm 0.5$ | $+0.1 \pm 0.1$ | 0.6 | $-7.5 \pm 6.7$ | $+1066.1 \pm 39.3$ | $+0.1 \pm 0.2$ | 1033.5 |
| **B** | $+0.0 \pm 0.0$ | $-0.3 \pm 0.0$ | $+0.0 \pm 0.0$ | 0.3 | $-0.2 \pm 0.2$ | $+24.4 \pm 0.9$ | $+0.0 \pm 0.0$ | 23.6 |
| **C** | $+0.0 \pm 0.0$ | $-0.3 \pm 0.0$ | $+0.0 \pm 0.0$ | 0.3 | $-0.2 \pm 0.2$ | $+24.6 \pm 0.9$ | $+0.0 \pm 0.0$ | 23.9 |
| **D** | $+0.0 \pm 0.2$ | $-0.8 \pm 0.4$ | $+0.1 \pm 0.1$ | 0.8 | $-7.7 \pm 6.9$ | $+1090.7 \pm 40.2$ | $+0.1 \pm 0.2$ | 1057.4 |

**(a)** June

| | Cannonball | | | | Paneled | | | |
|---|---|---|---|---|---|---|---|---|
| | Radial | Along-track | Cross-track | RMSE | Radial | Along-track | Cross-track | RMSE |
| **A** | $+0.2 \pm 12.4$ | $-36.4 \pm 25.1$ | $+0.0 \pm 0.5$ | 40.3 | $+0.3 \pm 23.7$ | $-61.8 \pm 47.7$ | $+0.0 \pm 0.9$ | 70.3 |
| **B** | $+0.1 \pm 2.9$ | $-12.2 \pm 5.9$ | $+0.0 \pm 0.1$ | 12.7 | $+0.1 \pm 6.1$ | $-11.6 \pm 12.4$ | $+0.0 \pm 0.2$ | 14.6 |
| **C** | $+0.1 \pm 2.9$ | $-12.6 \pm 6.0$ | $+0.0 \pm 0.1$ | 13.1 | $+0.1 \pm 6.2$ | $-20.1 \pm 12.8$ | $+0.0 \pm 0.2$ | 21.8 |
| **D** | $+0.2 \pm 9.5$ | $-49.0 \pm 19.8$ | $+0.0 \pm 0.4$ | 50.0 | $+0.4 \pm 17.5$ | $-81.9 \pm 36.3$ | $+0.0 \pm 0.6$ | 84.1 |

**(b)** September

reveals how the cannonball cannot account for asymmetry; with symmetric accelerations, no secular changes occur. Interestingly, the large cross-track acceleration does not lead to a large cross-track difference in the final position. Positions with constant and DLAM-1 albedo ($\mathbf{B}$ and $\mathbf{C}$) do not differ significantly.

For the September arc, the cannonball and paneled targets give more similar results. Again, the largest secular difference is in the along-track position. However, in contrast to the June arc, LRO is shifted back in the track this time. Due to the large variations in radial and along-track accelerations over each orbit, there are large periodic variations in the radial and along-track positions too. For the paneled target with solar and lunar radiation ($\mathbf{D}$), these have amplitudes of $18\,\mathrm{m}$ and $36\,\mathrm{m}$ for the radial and along-track differences, respectively. The periodic variations have higher amplitudes when not

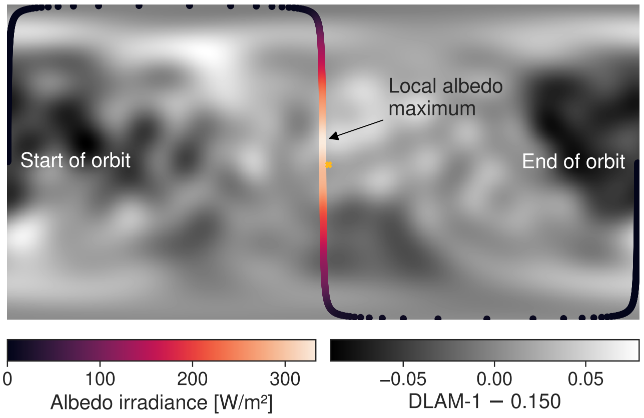


**Figure 13.** Ground track for September arc, colored by the irradiance due to DLAM-1 albedo. The map shows the difference between DLAM-1 and the constant albedo ($a = 0.150$). The maximum irradiance does not occur above the subsolar point (✖) but above the local albedo maximum 12° north of it.

including lunar radiation ($\mathbf{A}$), which otherwise cancel solar accelerations partially (see Section 4.2). There also is a $7\,\mathrm{m}$ RMSE difference for the paneled model in September between constant and DLAM-1 albedo, the only of the four cases where the choice of albedo model influences the final position.

These differences in position emphasize the importance of RP models for precise orbit determination. The best approximation of the true effect of RP is given by setup $\mathbf{D}$ (solar + lunar radiation) with a the paneled target. For both arcs, the maximum allowable total error would be exceeded by the superposition of secular and periodic variations if RP were neglected. The radial requirement of sub-meter accuracy would be violated by periodic variations alone.

### 4.4 Performance

Choosing the appropriate model is not only a consideration of accuracy but also one of computational effort. The aim is to find the most efficient model that is sufficiently accurate. To determine how much less efficient complex models like paneled targets or DLAM-1 are, we measured wall time durations for different model combinations. We ran each simulation 100 times in random order on a server with 2 Intel Xeon E5-2683 v3 CPUs (14 cores each, two threads per core with hyperthreading) while no other loads were present. 27 simulations ran in parallel such that all but one core were used. More parallelism would have triggered hyperthreading, which would have skewed measurements. Tudat was compiled in release configuration with GCC 7.5.0 at optimization level `-O2`. No other steps such as CPU pinning were taken. Note that software performance can be influenced by many, seemingly innocuous aspects [54]. Still, the results show the general tendency.

The wall time durations when including solar or lunar radiation are shown in Figure 14. Again, the baseline simulation without radiation serves as a reference. The median baseline time of $4.3\,\mathrm{min}$ includes computations for general integration and propagation, the lunar spherical harmonics gravity model, and point gravities from Sun and Earth. Solar radiation has a negligible complexity, even for a paneled target. Lunar radiation with constant albedo increases the duration by about $20\,\%$, but slightly more for the paneled than the cannonball target. These values depend highly on the number of source panels. The spherical harmonics expansion of DLAM-1 is computationally expensive and increases the duration by up to $80\,\%$ compared to the baseline. This is a significant performance penalty, which may not always be tolerable. Other authors even report increases of several hundred percent for DLAM-1 albedo [10].

The durations are relatively consistent as indicated by the inter-quartile range of at most $5\,\mathrm{s}$. Still, all distributions have a long tail toward longer durations: the difference between maximum and median is between 9 and 21 times higher than the difference between minimum and median. This skewness is typical for software performance.

## 5 Conclusion

We described a collection of RP models of varying levels of complexity, then examined the differences in short-term orbital effects of RP on LRO between these models. There are large seasonal differences in the RP accelerations: for small $\beta$ (e.g., around September), the accelerations are mainly radial and along-track, while they are predominantly cross-track for $\beta \approx \pm 90°$ (e.g., around June). After 2.5 days, the position diverged from the no-RP baseline by $1100\,\mathrm{m}$ in June and $80\,\mathrm{m}$ in September. Periodic variations of up to $40\,\mathrm{m}$ are superimposed on the secular differences over one orbital revolution. In September, the periodic variations are damped by lunar accelerations that oppose solar accelerations. Large differences also exist between the representations of LRO as a cannonball and a paneled target: due to the cannonball's symmetry, accelerations are more uniform and generally smaller than those of a paneled target, which can have the solar array track the Sun. Asymmetric effects, which a cannonball cannot represent, can lead to qualitative differences. Thermal radiation dominates the lunar emissions, and a constant albedo distribution is both sufficiently accurate and computationally cheaper than the spherical harmonics expansion DLAM-1.

Our results showed that RP is essential for precise orbit determination. Both the total and radial accuracy requirements of LRO would be violated otherwise. However,

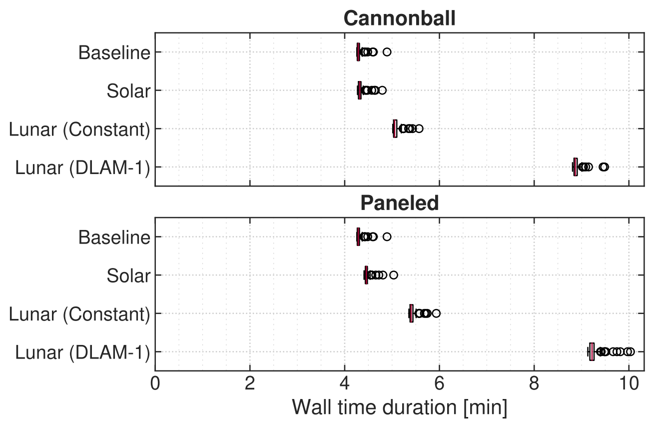


**Figure 14.** Wall time duration of simulations with different RP models. The statistics come from 100 runs for each model. Evaluation of DLAM-1's spherical harmonics expansion increases the duration by up to $80\,\%$.

not all models are worth the computational effort. We recommend the following setup:

- Solar radiation should be included since it is significant yet computationally cheap.
- Lunar thermal and constant albedo radiation should be included since it only increases walltime duration by 20 % and affects secular and periodic variations significantly. To reduce the performance impact, fewer rings could be used, although the lunar irradiance may then be underestimated.
- The spatial variations in albedo from DLAM-1 do not increase the accuracy much despite the performance penalty of 80 %. Therefore, it should not be included unless the utmost accuracy is desired (particularly in September). The spherical harmonics expansion could also be truncated to improve performance.
- The paneled target should be included since the cannonball underestimates accelerations and does not account for Sun tracking of the solar array. The performance impact of the paneled target is negligible.
- The cannonball target should only be included if its coefficient is estimated since a constant coefficient cannot represent changes in geometry and orientation. Even then, consistent estimation of the coefficient is difficult at small $\beta$ [7].

While we restricted our investigation to a small number of relatively simple models, the short-term orbital effect of these more involved models should also be investigated:

- Self-shadowing, particularly for solar radiation, can reduce the effective cross-section by up to 40 % for large $\beta$ [9].
- Moon topography can advance eclipse onset by up to 480 s for $\beta > 70°$ [9]. The conical shadow model should be replaced by one that evaluates lines of sight based on topography.
- DLAM-1 was published in 1999 based on miscalibrated Clementine imagery, which overestimates the actual albedo. A new spherical harmonics model should be fitted from more recent, properly calibrated imagery.
- Accelerations due to thermal reradiation by the spacecraft itself can be significant. Instantaneous reradiation should be replaced by a model that accounts for heating and conduction.
- The lunar opposition effect increases albedo radiation for low phase angles much more than Lambertian reflectance predicts. Such phase angles occur for small $\beta$. The Hapke BRDF with spatially resolved parameter maps [39] should be used for albedo reflection.
- Post-sunset lunar thermal radiation is underestimated because gradual cooling to nighttime temperatures is not reflected in our thermal model. It should be replaced with a more physical model due to the large magnitude of thermal compared to albedo radiation.

## Code availability

The code is available at https://github.com/DominikStiller/tudelft-hpb-project.

## References


1. O. Montenbruck and E. Gill, *Satellite Orbits*. Springer Berlin Heidelberg, Dec. 2000, 371 pp. DOI: 10.1007/978-3-642-58351-3.
2. C. R. Tooley *et al.*, “Lunar Reconnaissance Orbiter mission and spacecraft design,” *Space Science Reviews*, vol. 150, no. 1-4, pp. 23–62, Jan. 2010. DOI: 10.1007/s11214-009-9624-4.
3. G. Chin *et al.*, “Lunar Reconnaissance Orbiter overview: The instrument suite and mission,” *Space Science Reviews*, vol. 129, no. 4, pp. 391–419, May 2007. DOI: 10.1007/s11214-007-9153-y.
4. M. T. Zuber *et al.*, “The Lunar Reconnaissance Orbiter laser ranging investigation,” *Space Science Reviews*, vol. 150, no. 1-4, pp. 63–80, May 2009. DOI: 10.1007/s11214-009-9511-z.
5. S. Slojkowski, J. Lowe, and J. Woodburn, “Orbit determination for the Lunar Reconnaissance Orbiter using an extended Kalman filter,” in *International Symposium on Space Flight Dynamics (ISSFD) 2015*, 2015.
6. R. Floberghagen, P. Visser, and F. Weischede, “Lunar albedo force modeling and its effect on low lunar orbit and gravity field determination,” *Advances in Space Research*, vol. 23, no. 4, pp. 733–738, Jan. 1999. DOI: 10.1016/s0273-1177(99)00155-6.
7. S. E. Slojkowski, “Lunar Reconnaissance Orbiter orbit determination accuracy analysis,” in *International Symposium on Space Flight Dynamics*, 2014.
8. E. Mazarico *et al.*, “Orbit determination of the Lunar Reconnaissance Orbiter,” 3, vol. 86, Springer Science and Business Media LLC, Sep. 2011, pp. 193–207. DOI: 10.1007/s00190-011-0509-4.
9. E. Mazarico, G. A. Neumann, M. K. Barker, S. Goossens, D. E. Smith, and M. T. Zuber, “Orbit determination of the Lunar Reconnaissance Orbiter: Status after seven years,” *Planetary and Space Science*, vol. 162, pp. 2–19, Nov. 2018. DOI: 10.1016/j.pss.2017.10.004.
10. A. Nicholson, S. Slojkowski, A. Long, M. Beckman, and R. Lamb, “NASA GSFC Lunar Reconnaissance Orbiter (LRO) orbit estimation and prediction,” in *SpaceOps 2010 Conference*, American Institute of Aeronautics and Astronautics, Apr. 2010. DOI: 10.2514/6.2010-2328.
11. D. Smith, M. Zuber, F. Lemoine, M. Torrence, and E. Mazarico, “Orbit determination of LRO at the Moon,” in *7th Int. Laser Ranging Service Workshop*, 2008, pp. 13–17.
12. S. Bauer *et al.*, “Demonstration of orbit determination for the Lunar Reconnaissance Orbiter using one-way laser ranging data,” *Planetary and Space Science*, vol. 129, pp. 32–46, Sep. 2016. DOI: 10.1016/j.pss.2016.06.005.
13. A. Maier and O. Baur, “Orbit determination and gravity field recovery from Doppler tracking data to the Lunar Reconnaissance Orbiter,” *Planetary and Space Science*, vol. 122, pp. 94–100, Mar. 2016. DOI: 10.1016/j.pss.2016.01.014.

14. K. Vielberg and J. Kusche, "Extended forward and inverse modeling of radiation pressure accelerations for LEO satellites," *Journal of Geodesy*, vol. 94, no. 4, Mar. 2020. DOI: 10.1007/s00190-020-01368-6.

15. G. Kopp and J. L. Lean, "A new, lower value of total solar irradiance: Evidence and climate significance," *Geophysical Research Letters*, vol. 38, no. 1, Jan. 2011. DOI: 10.1029/2010gl045777.

16. C. J. Wetterer *et al.*, "Refining space object radiation pressure modeling with bidirectional reflectance distribution functions," *Journal of Guidance, Control, and Dynamics*, vol. 37, no. 1, pp. 185–196, Jan. 2014. DOI: 10.2514/1.60577.

17. O. Montenbruck, P. Steigenberger, and U. Hugentobler, "Enhanced solar radiation pressure modeling for Galileo satellites," *Journal of Geodesy*, vol. 89, no. 3, pp. 283–297, Nov. 2014. DOI: 10.1007/s00190-014-0774-0.

18. M. Ziebart, "Generalized analytical solar radiation pressure modeling algorithm for spacecraft of complex shape," *Journal of Spacecraft and Rockets*, vol. 41, no. 5, pp. 840–848, Sep. 2004. DOI: 10.2514/1.13097.

19. A. Prša *et al.*, "Nominal values for selected solar and planetary quantities: IAU 2015 Resolution B3," *The Astronomical Journal*, vol. 152, no. 2, p. 41, Aug. 2016. DOI: 10.3847/0004-6256/152/2/41.

20. G. Kopp, "Magnitudes and timescales of total solar irradiance variability," *Journal of Space Weather and Space Climate*, vol. 6, A30, 2016. DOI: 10.1051/swsc/2016025.

21. S. Dewitte and N. Clerbaux, "Measurement of the Earth radiation budget at the top of the atmosphere—a review," *Remote Sensing*, vol. 9, no. 11, p. 1143, Nov. 2017. DOI: 10.3390/rs9111143.

22. P. Knocke, J. Ries, and B. Tapley, "Earth radiation pressure effects on satellites," in *Astrodynamics Conference*, American Institute of Aeronautics and Astronautics, Aug. 1988. DOI: 10.2514/6.1988-4292.

23. G. Heiken and B. M. French, *Lunar Sourcebook, A User's Guide to the Moon*. Cambridge University Press, 1991.

24. C. J. Rodriguez-Solano, U. Hugentobler, P. Steigenberger, and S. Lutz, "Impact of Earth radiation pressure on GPS position estimates," *Journal of Geodesy*, vol. 86, no. 5, pp. 309–317, Oct. 2011. DOI: 10.1007/s00190-011-0517-4.

25. F. Wöske, T. Kato, B. Rievers, and M. List, "GRACE accelerometer calibration by high precision non-gravitational force modeling," *Advances in Space Research*, vol. 63, no. 3, pp. 1318–1335, Feb. 2019. DOI: 10.1016/j.asr.2018.10.025.

26. P. Knocke, "Earth radiation pressure effects on satellites," Ph.D. dissertation, The University of Texas at Austin, 1989.

27. F. G. Lemoine *et al.*, "High–degree gravity models from GRAIL primary mission data," *Journal of Geophysical Research: Planets*, vol. 118, no. 8, pp. 1676–1698, Aug. 2013. DOI: 10.1002/jgre.20118.

28. P. R. Goode *et al.*, "Earthshine observations of the Earth's reflectance," *Geophysical Research Letters*, vol. 28, no. 9, pp. 1671–1674, May 2001. DOI: 10.1029/2000gl012580.

29. A. Hattori and T. Otsubo, "Time-varying solar radiation pressure on Ajisai in comparison with LAGEOS satellites," *Advances in Space Research*, vol. 63, no. 1, pp. 63–72, Jan. 2019. DOI: 10.1016/j.asr.2018.08.010.

30. J. Marshall, S. Luthcke, P. Antreasian, and G. Rosborough, "Modeling radiation forces acting on TOPEX/Poseidon for precision orbit determination," Goddard Space Flight Center, Tech. Rep. NASA-TM-104564, 1992.

31. E. Mazarico, M. T. Zuber, F. G. Lemoine, and D. E. Smith, "Effects of self-shadowing on nonconservative force modeling for Mars-orbiting spacecraft," *Journal of Spacecraft and Rockets*, vol. 46, no. 3, pp. 662–669, May 2009. DOI: 10.2514/1.41679.

32. P. W. Kenneally and H. Schaub, "Fast spacecraft solar radiation pressure modeling by ray tracing on graphics processing unit," *Advances in Space Research*, vol. 65, no. 8, pp. 1951–1964, Apr. 2020. DOI: 10.1016/j.asr.2019.12.028.

33. D. A. Vallado and J. Wertz, *Fundamentals of Astrodynamics and Applications, 4th ed.* Microcosm Press, 2013, p. 1106.

34. R. Zhang, R. Tu, P. Zhang, J. Liu, and X. Lu, "Study of satellite shadow function model considering the overlapping parts of Earth shadow and Moon shadow and its application to GPS satellite orbit determination," *Advances in Space Research*, vol. 63, no. 9, pp. 2912–2929, May 2019. DOI: 10.1016/j.asr.2018.02.002.

35. Z. Li, M. Ziebart, S. Bhattarai, and D. Harrison, "A shadow function model based on perspective projection and atmospheric effect for satellites in eclipse," *Advances in Space Research*, vol. 63, no. 3, pp. 1347–1359, Feb. 2019. DOI: 10.1016/j.asr.2018.10.027.

36. USGS Astrogeology Science Center. "Moon Clementine UVVIS global mosaic 118m v2." (Apr. 9, 2009), [Online]. Available: https://astrogeology.usgs.gov/search/map/Moon/Clementine/UVVIS/Lunar_Clementine_UVVIS_750nm_Global_Mosaic_118m_v2.

37. A. R. Vasavada *et al.*, "Lunar equatorial surface temperatures and regolith properties from the Diviner lunar radiometer experiment," *Journal of Geophysical Research: Planets*, vol. 117, no. E12, Apr. 2012. DOI: 10.1029/2011je003987.

38. P. O. Hayne *et al.*, "Global regolith thermophysical properties of the Moon from the Diviner lunar radiometer experiment," *Journal of Geophysical Research: Planets*, vol. 122, no. 12, pp. 2371–2400, Dec. 2017. DOI: 10.1002/2017je005387.

39. H. Sato, M. S. Robinson, B. Hapke, B. W. Denevi, and A. K. Boyd, "Resolved Hapke parameter maps of the Moon," *Journal of Geophysical Research: Planets*, vol. 119, no. 8, pp. 1775–1805, Aug. 2014. DOI: 10.1002/2013je004580.

40. A. McEwen and M. Robinson, "Mapping of the Moon by Clementine," *Advances in Space Research*, vol. 19, no. 10, pp. 1523–1533, Jan. 1997. DOI: 10.1016/s0273-1177(97)00365-7.

41. Y. Shkuratov, V. Kaydash, V. Korokhin, Y. Velikodsky, N. Opanasenko, and G. Videen, "Optical measurements of the Moon as a tool to study its surface," *Planetary and Space Science*, vol. 59, no. 13, pp. 1326–1371, Oct. 2011. DOI: 10.1016/j.pss.2011.06.011.

42. M. Iqbal, *Introduction to Solar Radiation*. Academic Press Canada, 1983.

43. B. J. Buratti, J. K. Hillier, and M. Wang, "The lunar opposition surge: Observations by Clementine," *Icarus*, vol. 124, no. 2, pp. 490–499, Dec. 1996. DOI: 10.1006/icar.1996.0225.

44. B. Hapke, *Theory of reflectance and emittance spectroscopy*. Cambridge University Press, 2012.

45. R. S. Park *et al.*, "Estimating a high-resolution lunar gravity field and time-varying core signature," in *AGU Fall Meeting Abstracts*, vol. 2011, Dec. 2011, P44B-06, P44B–06.

46. J. L. Bandfield, P. O. Hayne, J.-P. Williams, B. T. Greenhagen, and D. A. Paige, "Lunar surface roughness derived from LRO Diviner radiometer observations," *Icarus*, vol. 248, pp. 357–372, Mar. 2015. DOI: 10.1016/j.icarus.2014.11.009.

47. NASA Science Mission Directorate. "Spacecraft icons." (2018), [Online]. Available: https://science.nasa.gov/get-involved/toolkits/spacecraft-icons.

48. M. Mesarch, M. Beckman, D. Folta, R. Lamb, and K. Richon, "Maneuver operations results from the Lunar Reconnaissance Orbiter (LRO) mission," in *SpaceOps 2010 Conference*, American Institute of Aeronautics and Astronautics, Apr. 2010. DOI: 10.2514/6.2010-1985.

49. A. Löcher and J. Kusche, "Precise orbits of the Lunar Reconnaissance Orbiter from radiometric tracking data," *Journal of Geodesy*, vol. 92, no. 9, pp. 989–1001, Feb. 2018. DOI: 10.1007/s00190-018-1124-4.

50. W. M. Folkner, J. G. Williams, and D. H. Boggs, "The planetary and lunar ephemeris DE 421," *IPN progress report*, vol. 42, no. 178, p. 1, 2009.

51. B. A. Archinal *et al.*, "Report of the IAU working group on cartographic coordinates and rotational elements: 2009," *Celestial Mechanics and Dynamical Astronomy*, vol. 109, no. 2, pp. 101–135, Dec. 2010. DOI: 10.1007/s10569-010-9320-4.

52. Goddard Space Flight Center, "A standardized lunar coordinate system for the Lunar Reconnaissance Orbiter and lunar datasets, Lro project and lgcwg white paper," Tech. Rep., Oct. 1, 2008.

53. S. Goossens, Á. F. Mora, E. Heijkoop, and T. J. Sabaka, "Patched local lunar gravity solutions using GRAIL data," *Earth and Space Science*, vol. 8, no. 11, Oct. 2021. DOI: 10.1029/2021ea001695.

54. T. Mytkowicz, A. Diwan, M. Hauswirth, and P. F. Sweeney, "Producing wrong data without doing anything obviously wrong!" *ACM SIGPLAN Notices*, vol. 44, no. 3, pp. 265–276, Feb. 2009. DOI: 10.1145/1508284.1508275.